Journal of

Computation and Artificial Intelligence in Mechanics and Biomechanics

Editor in Chief:
Jorge Belinha

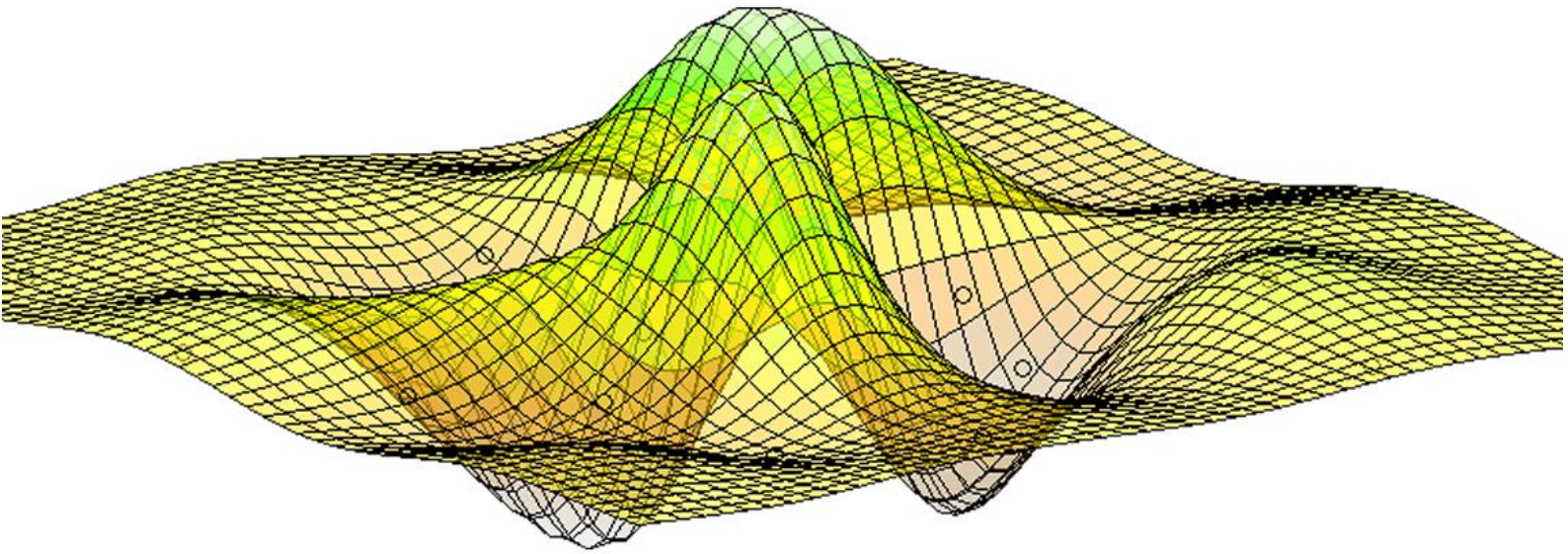

ISSN 2184-8971
Volume 1, Issue 3

PUBLICAÇÕES ISEP
European Commission | Horizon 2020 European Union funding for Research & Innovation
OpenAIRE
zenodo

Journal of Computation and Artificial Intelligence in Mechanics and Biomechanics

Editorial overview by
Editor in chief: Jorge Belinha [1]

[1]*School of Engineering, Polytechnic of Porto (ISEP), Department of Mechanical Engineering, Portugal, job@isep.ipp.pt*

Journal of Computation and Artificial Intelligence in Mechanics and Biomechanics (JCAIMB) is a scholarly online peer review free open access journal fully sponsored by "Publicações ISEP". All manuscripts are available in the ZENODO repository database, from OpenAIRE project, allowing an automatically abstracting and indexation and free open access.

Thus, JCAIMB is committed to ensure free Open Science to both authors and readers and to publish only quality works, which are reviewed by experts in related field. Moreover, JCAIMB aims to publish quality original research works, following the scientific method of scholarly value in computational mechanics and biomechanics combined with several degrees of artificial intelligence, whose formulations and applications are properly demonstrated and validated. Nevertheless, innovative applications using commercial software packages are encouraged, as well as original and up-to-date revision manuscripts. In this issue, four manuscripts are published in JCAIMB:

- A stress analysis with the finite element method of a tibia model with a bone callus, by Andreia Oliveira and Jorge Belinha;
- Cupula response to otoconia debris in the semicircular canal, by Carla F. Santos, Jorge Belinha, Fernanda Gentil, Marco Parente and Renato Natal Jorge;
- The computational simulation and impact analysis of the rib bones, by Dilki Dias and Jorge Belinha;
- Development of a DoE with a new electrospinning system for cartilage tissue engineering, by Eduarda Silva, Angela. Semitela, Paula A.A.P. Marques and António Completo.

Enjoy.

The editorial team.

Technical information:

Publisher:	Publicações ISEP - https://publicacoes.isep.ipp.pt/
Repository:	ZENODO repository database - https://zenodo.org/
Licence:	under the terms of the Creative Commons Attribution 4.0 International (CC BY 4.0) license.
Director:	Jorge Belinha
Email:	job@isep.ipp.pt
Format:	Online: https://publicacoes.isep.ipp.pt/jcaimb
Periodicity:	Semestrial

Journal of Computation and Artificial Intelligence in Mechanics and Biomechanics ISSN 2184-8971
Volume 1, Issue 3, Page 58-63, 2021

A stress analysis with the finite element method of a tibia model with a bone callus

Andreia Oliveira[1], Jorge Belinha[2]

[1] *School of Engineering, Polytechnic of Porto, 1151379@isep.ipp.pt; R. Dr. António Bernardino de Almeida 431;Porto;Portugal*
[2] *School of Engineering, Polytechnic of Porto, job@isep.ipp.pt; R. Dr. António Bernardino de Almeida 431;Porto;Portugal*

Abstract
Human tibial fractures are complex injuries that usually result in long periods of hospitalization and rehabilitation. During the slow healing process, the bone callus gradually increases its mechanical properties. The aim of this work is to evaluate the structural influence of the gradual mechanical properties of a callus bone due to a transverse tibial fracture. Thus, a 2D tibia model was constructed and analysed using the finite element method (FEM). At the transverse fracture site, a bone callus was considered. In order to simulate the healing process, four distinct Young's moduli were assumed for the bone callus, ranging between the soft callus (250 MPa) and hard callus (6000 MPa) stages. All materials were assumed homogeneous, isotropic, and linear elastic. Distinct geometries and load cases were considered, simulating a normal alignment and malalignment conditions, such as a valgus and a varus knee. Each model was analysed with FEM assuming an elasto-static analysis and using constant strain triangular elements. Von Mises effective stress and principal stress fields were obtained for each model. The obtained results show that, compared to the aligned condition, both malalignment conditions induce the highest stress levels in the model. The maximum stresses were observed in the tibia model with the 250 MPa callus and gradually decreased with the increase of the mechanical properties of the callus.

***DOI**: 10.5281/zenodo.5710378*

Article Info

Keywords
Tibia
Transverse fracture
Bone callus
Finite element method
Biomechanics

Article History
Received: *14/12/2020*
Revised: *12/03/2021*
Accepted: *12/05/2021*

1 Introduction

The skeletal system is formed by living tissues that support the other tissues of the human body, however its integrity can be compromised when fractures occur. The prediction of fracture healing remains one of the major challenges [1]. Among long bones, tibial fractures are the most common fractures and usually result in long periods of hospitalization and rehabilitation [2]. The conventional method of assessing fracture healing in long bones is by a combination of passive manipulation of the injured limb, to access the strength of the fracture, along with medical imaging to determine the volume and state of fracture-binding tissues, referred to as callus. However, this assessment method is subjective and unanimity lacks among clinicians [3]. Even though there is no consensus when a fracture is consolidated, clinical studies and individual patient assessment require a measurable definition that indicates the end of the consolidation. Thus, in research environment, there has been a need for objective, quantitative and simulation methods that allow monitoring the consolidation of the fracture, assisting the diagnosis and treatment of delayed unions and non-unions, as well as helping to identify the endpoint of healing, avoiding prolonged treatments.

One of the most notable features of living tissue is its ability to self-regenerate [4]. The healing process strongly depends on the mechanical actions on the callus, which determine the relative movement of the bone fragments. It is a complex process involving cellular differentiation, strongly stimulated by mechanical loading [4]. Knowledge of the mechanisms involved and their interdependencies with external factors supports the understanding of the accelerated regeneration processes and the success of rehabilitation [4]. The fractured bone is immobilized using a specific method to repair and restore its main function. In this process, the bone goes through four main phases: inflammation, soft callus formation, hard callus formation and bone remodelling. The healing process can be influenced by certain factors that can be divided in two categories: systemic factors such as age, pathologies or external factors, and local factors such as the degree of fracture, type of bone, blood supply, degree of vascularity and mechanical factors [4].

Mechanical stress or strain in fracture sites are typically estimated using finite element analysis (FEA). The Finite Element Method (FEM) is the most frequently used numeric tool for the analysis of bone architectures in structural mechanics. When a structure is loaded, stresses are generated in its constituent materials, characterized by their

Corresponding Author:
Jorge Belinha
job@isep.ipp.pt

magnitude and orientation, and by their distribution along the structure volume [5]. Those attributes depend not only on the constituent materials' properties and their spatial and geometric organization, but also on the intensity and position of the applied loads, and the system's boundary conditions [5]. Each element is associated with a material and a geometric shape, which define its stiffness. By assembling the stiffness matrix of all elements, it is possible to construct the global stiffness matrix of the model, $\boldsymbol{K}$, in which are imposed the essential boundary conditions. The natural boundary conditions (external forces), $\boldsymbol{F}$, are defined and the system of equations is established: $\boldsymbol{KU} = \boldsymbol{F}$, which allows to determine the displacement field, $\boldsymbol{U}$. FEM allows the division of a complex problem by discretizing the global structure into several simpler polygonal elements. The FEM is a useful tool to assess mechanical stimuli within healing fractures that cannot be measured directly during experimental investigations. Therefore, to simulate the consolidation process, the mechanical properties of the callus in its different phases must be known and reproduced. Although there are many studies in the literature on sheep and rat bone healing [6,7], some data can be found on callus stiffness in humans, as observed in Nikiforidis et al. [8] and Claes and Cunningham [9]. The approximate values of the Young's modulus of tissues can be found in numerical studies on bone consolidation simulation, in Milan et al. [10], Byrne et al. [11], Lacroix et al. [12] and Mehboob et al. [13]. In another study, some materials were used to simulate the consolidation phases [14].

This work aims to study how the variation of the Young's modulus of the bone callus (due to a transverse tibial fracture) influences the stress field in the healing fracture vicinity. Thus, the mechanical response of the tibia model, with a callus possessing distinct mechanical properties, is analysed using the finite element method. Furthermore, it is investigated how the geometry of the tibia, combined with the presence of a bone callus, influences the stress magnitude and distribution. Therefore, three models of the tibia were constructed, each one possessing its own load case: a normal tibia showing a normal alignment and two malalignment conditions, such as a valgus and a varus knee.

2 Materials and Methods

Three 2D models of the tibia bone were constructed in FEMAP© software (student version). The 2D models were obtained from anonymized radiographs of an adult male healthy individual, an adult male individual possessing the valgus malalignment condition and an adult male individual possessing the varus malalignment condition. All the models represent a left tibia model. A knee that is perfectly aligned has its load-bearing axis on a line that runs down the middle of the leg, through the hip, knee, and ankle. If the knee is not perfectly aligned, it is described as either valgus (knock-kneed), if the distal part is more lateral, or varus (bowlegged), if the distal part is more medial.

The three 2D models possess the same number of nodes and elements: 2461 nodes and 4574 triangular elements (constant strain elements). After the construction of the models, the corresponding node/element mesh was imported to the "Finite Element and Meshless Methods Analysis Software", FEMAS©, an academic freeware using MATLAB© environment (cmech.webs.com). All the models possess at the middle of the tibial diaphysis a transverse fracture, which was filled with callus material. The material properties and the essential and natural boundary conditions are inserted in FEMAS. The model is composed of two distinct materials: the homogeneous bone tissue and the callus. In this work, the homogenized bone tissue assumed the mechanical properties of a cortical bone. The mechanical properties of each one of the materials are represented in Table 1, in which it is possible to visualize the four different Young's moduli that were considered for the callus. The intention is to have the representative behaviour of each healing stage, in a range of elasticity values that vary between the soft callus, until a phase that represents the hard callus stage. Both Young's modulus (E) and Poisson's coefficient (υ) were obtained from the literature. All materials were assumed to be homogeneous, isotropic, and linear elastic.

Table 1 - Mechanical properties of the materials [12].

Material	Young's modulus (MPa)	Poisson's coefficient
Homogenized Bone Tissue	16700	0.3
Callus 1 (Cartilage)	250	0.4999
Callus 2 (Intermediate bone)	1500	0.4999
Callus 3 (Mature bone)	4000	0.4999
Callus 4 (Mature bone)	6000	0.4999

Regarding the essential boundary conditions (displacements constrains), the model was fixed in the distal extremity, with no displacement allowed in any of the directions of the two degrees-of-freedom. Concerning the natural boundary conditions (external forces), this work intends to analyse a peak load during walking for an approximately 80kg human being. Thus, assuming that the individual is standing in one leg, all the load is applied to the proximal tibia distributed

into a $10 \times 10\ mm^2$ surface. For the 2D analysis, is was considered the plane strain deformation theory. Thus, only a 2D slice with $1mm$ thickness was analysed. The load on that $1mm$ thickness was distributed at the proximal tibia (thus, only 1/10 of the total load). In this work, three 2D models were constructed, each one representing a health condition: normal alignment (case 1), 10º valgus malalignment (case 2) and 10º varus malalignment (case 3). Each one of these models will possess its own load. Therefore, for the normal alignment (case 1) it was considered: $\vec{F}_1 = \{0{,}80\}^T\ N$, for 10º valgus malalignment (case 2) it was assumed: $\vec{F}_2 = \{13.89, -78.78\}^T N$ and for 10º varus malalignment (case 3) it was considered: $\vec{F}_3 = \{-13.89, -78.78\}^T N$.

3 Numerical Results

The models described previously were analysed with FEM and the stress fields of the von Mises effective stress, σ_{ef}, and the principal stresses, σ_1 and σ_2, were calculated. In Fig.1, for each bone callus and each geometric model, the obtained stress distribution maps are shown.

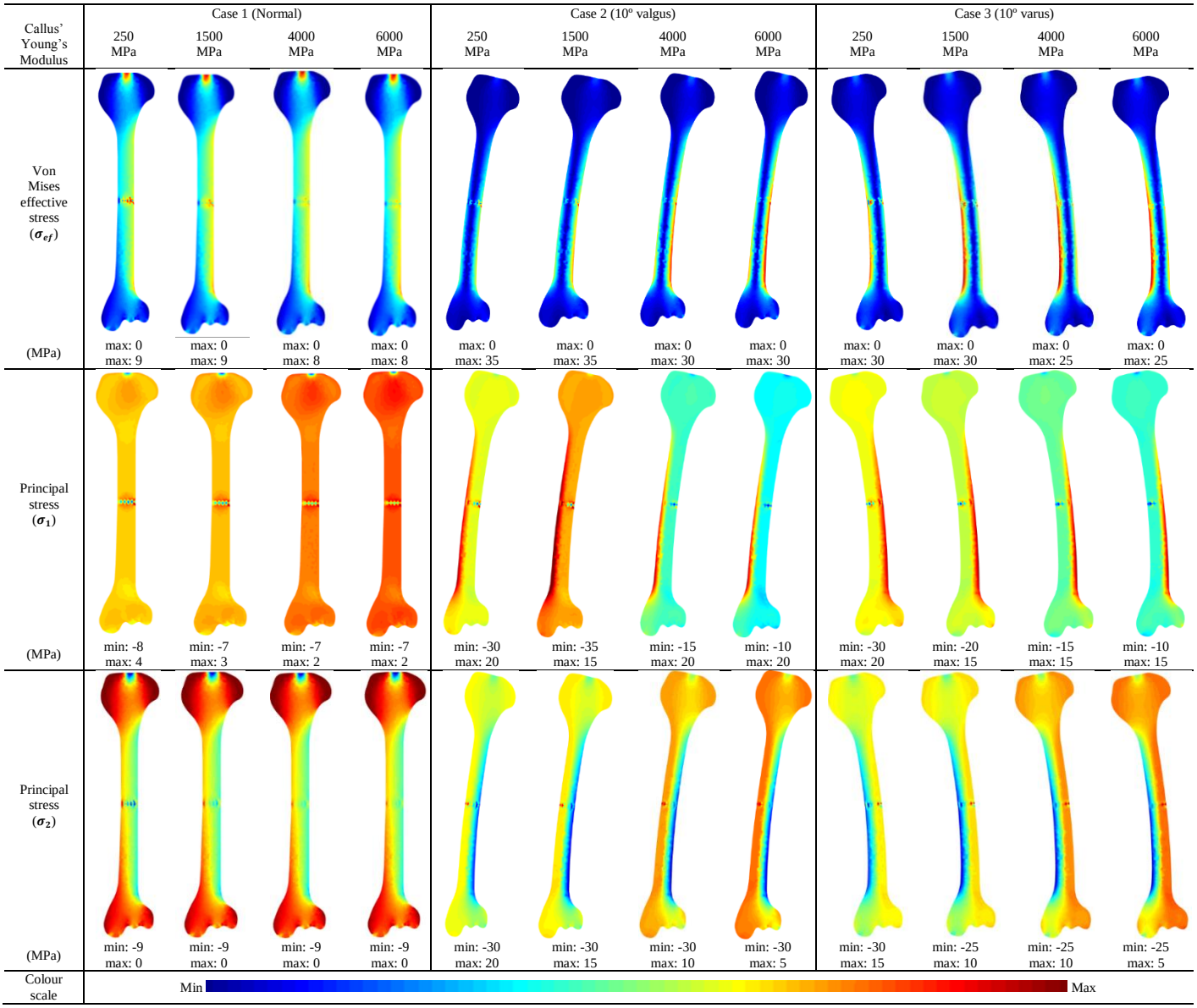

Fig.1 – Stress maps obtained with each model case: von Mises effective stresses (σ_{ef}) and principal stresses (σ_1 *and* σ_2) for each callus.

Fig.2 shows the average stress at the bone callus. The average stresses were obtained with: $\bar{\sigma} = n^{-1} \sum_{i=1}^{n} \sigma_i$, being n the number of elements belonging to the bone callus area and σ_i the stress on element i (belonging to the bone callus). In

Fig.3, the stress variation along two region lines (region 1 represent the lateral zone of the diaphysis and region 2 represents the medial zone of the diaphysis) is shown for each bone callus and each geometric model.

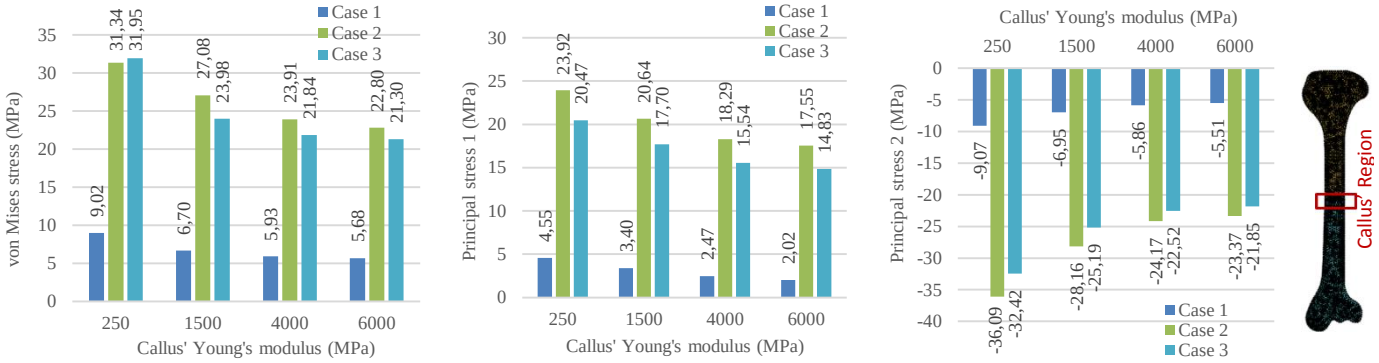

(a) (b) (c)

Fig.2 – Average values at the callus' region for each case: von Mises effective stress σ_{ef} (a), principal stress σ_1 (b), principal stress σ_2 (c).

4 Discussion

In this work, the main goal was to understand the mechanical behaviour of the tibia with a callus of different mechanical properties that simulate the healing process. Furthermore, the influence of the geometry was also investigated, by analysing models presenting normal alignment and malalignment conditions, such as a valgus and a varus knee. Twelve models were constructed and analysed with FEM (three distinct geometries in which the Young's modulus of the bone callus was varied four times between 250MPa and 6000MPa). The FEM allowed to obtain the stress fields of each model, corresponding to the von Mises effective stress, σ_{ef}, and the principal stresses, σ_1 and σ_2. The von Mises stress is a yield criterion that evaluates the maximum distortion energy of a material: a material starts to fail when the von Mises stress value approaches the material characteristic yield strength [15]. In the colour maps of Fig.1, the highest von Mises stresses are concentrated in different regions, being the highest values found at the tibial diaphysis. Considering Fig.2(a) and focusing only in the callus' region, the maximum average von Mises stresses were observed in the tibia model with the 250 MPa callus and then, it gradually decreased with the increase of the bone callus Young's modulus. This observation is valid for three 2D models analysed. Fig.2 shows that the both valgus knee (case 2) and varus knee (case 3) present very close average stresses. With Fig.2 it is possible to understand that the malalignment conditions (case 2 and case 3) induce stresses 350%-400% higher than a normal alignment condition. Thus, it is expected that malalignment conditions require larger immobilization periods when compared with a normal alignment condition (higher stresses at the bone callus can induce further damage and re-inflammation). The same observations can be made when the principal stresses σ_1 and σ_2 are analysed. In a 2D model, the highest positive values of σ_1 represent the highest tensile stress and the highest negative value (absolute value) of σ_2 represent the highest compressive stress. Fig.1 shows that the valgus knee (case 2) induces higher tensile stresses at the medial line of the diaphysis and higher compressive stresses at the lateral line of the diaphysis. On the other hand, the varus knee (case 3) induces higher tensile stresses at the lateral line of the diaphysis and higher compressive stresses at the medial line of the diaphysis.

Fig.3 allows to visualize the stress distribution with detail in both lateral diaphysis line (region 1) and medial diaphysis line (region 2). Thus, considering the diaphysis regions of the tibia, the lateral line (region 1) presents higher stress in each of the load cases compared to the medial line (region 2). Thus, in the lateral region, case 1 (Fig.3), the maximum von Mises effective stress was 6.07 MPa, the principal stress σ_1 was 0.3 MPa (absolute) and principal stress σ_2 was 6.48 MPa (absolute). These values are observed near the distal extremity of the tibia, for all the models of the tibia with callus' Young's modulus from 250 to 6000 MPa. On the other hand, in case 2 (Fig.3), von Mises' maximum stress was higher in the callus region, particularly in the model with the callus possessing a Young's modulus of 250 MPa, with a peak of 29.92 MPa, as well as for the principal stress σ_2 of 31.46 MPa (absolute). Near the distal extremity of the tibia, a second peak was observed for von Mises' stress, σ_{ef}=29.62 MPa, and for the principal stress σ_2=30.41 MPa (absolute). For case 3 (Fig.3), the maximum peak is observed at the callus region, in which von Mises' stress reaches 19.54 MPa, principal stress σ_1 reaches 20.47 MPa and principal stress σ_2 achieves 2.02 MPa. These highest values are obtained for bone callus with a Young's modulus of 250 MPa.

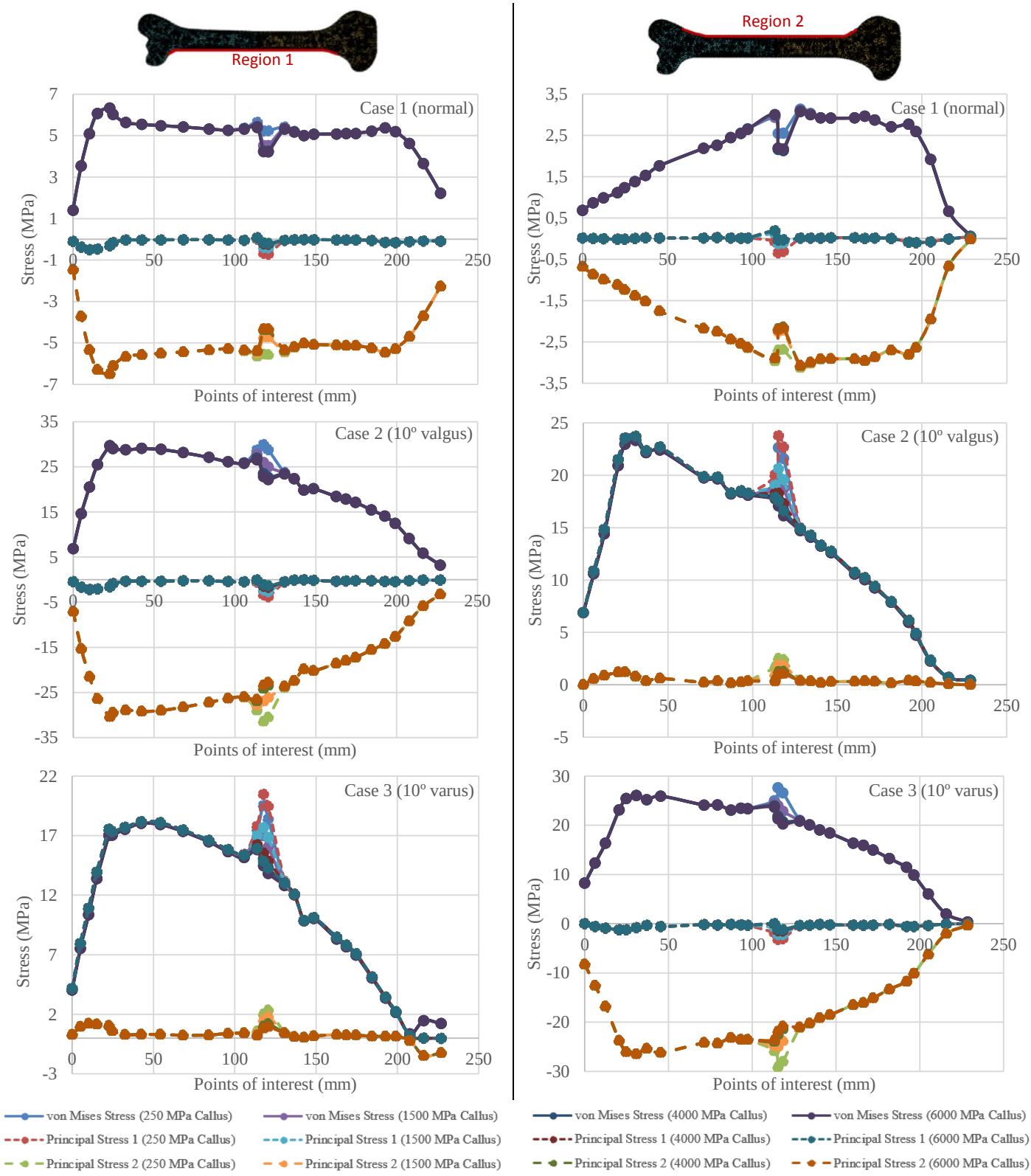

Fig.3 – Values of the von Mises effective stress σ_{ef}, principal stress σ_1 and principal stress σ_2, for each model case, at region lines.

Subsequently, for the medial region, case 1 (Fig.3), the maximum von Mises effective stress was 3.13 MPa, for all the models of the tibia regardless the Young's modulus of the callus bone, in the callus region. For the case 2 (Fig.3), the maximum von Mises effective stress was 23.33 MPa and maximum principal stress σ_1 of 23.71 MPa, near the distal extremity of the tibia, for all the models of the tibia with callus. In the callus region, it was observed a maximum von

Mises stress of 22.63 MPa and principal stress σ_1 of 23.77 MPa, for the model with the callus' Young's modulus of 250 MPa. Lastly, in case 3 (Fig.3), the maximum stresses are obtained for the bone callus possessing a Young's modulus of 250 MPa. Thus, a maximum von Mises' stress of 27.63 MPa is observed and a principal stress σ_1 of 3.22 MPa (absolute) and principal stress σ_2 of 29.1 MPa (absolute).

5 Conclusions

Tibia is one of the most important long bone and the main weight-bearing bone of the human leg, being responsible for receiving the body weight and transmit it to the foot when a human being stands or walks. A 2D simulation was performed aiming to obtain the stress distribution in the tibia. In order to perform the computational simulation, several approximations were assumed to simplify the model, e.g. the bone was considered isotropic and the FEM analysis was performed assuming the 2D plane strain deformation theory (2D-PSDT). These simplifications only allow to approximate the solution. Nevertheless, since 2D-PSDT is a simplification of the full 3D deformation theory for a target observation plane, it is expected that the obtained 2D stress distributions are very close with the real 3D stress distributions in the observed plane. Thus, the obtained results allow to understand the stress distribution in the tibia bone and predict which locations are under higher stress levels. This work also shows how a material discontinuity, such as a bone callus, influences the stress distribution, as well as variations in the geometry of the tibia bone and in the material properties of the callus bone.

Acknowledgments

The authors truly acknowledge the funding provided by Ministério da Ciência, Tecnologia e Ensino Superior - Fundação para a Ciência e a Tecnologia (Portugal), and by LAETA, under project UIDB/50022/2020

References

[1] Sridevi M, Prakasam P, Kumaravel S, Madhava P. Tibia Fracture Healing Prediction Using First-Order Mathematical Model. Computational and Mathematical Methods in Medicine. 2015;1–9.
[2] Kim SH, Chang SH, Jung HJ. The finite element analysis of a fractured tibia applied by composite bone plates considering contact conditions and time-varying properties of curing tissues. Composite Structures. 2010;92(9):2109–2118.
[3] McClelland D, Thomas P, Bancroft G, Moorcraft CI. Fracture healing assessment comparing stiffness measurements using radiographs. Clinical Orthopaedics and Related Research. 2007;457:214–219.
[4] Flores A, Marques A, Machado J, Marta M, Vaz M. Bone Immobilization devices and consolidation mechanisms: Impact on healing time. Procedia Structural Integrity. 2017;5:34–39.
[5] Huiskes R, Chao EY. A survey of finite element analysis in orthopedic biomechanics: the first decade. J. Biomech. 1983;16(6):385–409.
[6] Floerkemeier T, Thorey F, Hurschler C, Wellmann M, Witte F., Windhagen H. Stiffness of callus tissue during distraction osteogenesis. Orthopaedics & Traumatology: Surgery & Research. 2010;96(2):155-160.
[7] Mora-Macias J, Reina-Romo E, Lopez-Pliego M, Giraldez-Sanchez MA, Dominguez J. In Vivo Mechanical Characterization of the Distraction Callus During Bone Consolidation. Annals of Biomedical Engineering. 2015;43(11):2663-2674.
[8] Nikiforidis G, Bezerianos A, Dimarogonas A, Sutherland C. Monitoring of fracture healing by lateral and axial vibration analysis. Journal of Biomechanics. 1990;23(4):323-330.
[9] Claes LE, Cunningham JL. Monitoring the mechanical properties of healing bone, Clinical Orthopedics and Related Research. 2009;467(8):1964-1971.
[10] Milan JL, Planell JA, Lacroix D. Simulation of bone tissue formation within a porous scaffold under dynamic compression. Biomechanics and Modeling in Mechanobiology. 2010;9(5):583–596.
[11] Byrne DP, Lacroix D, Prendergast PJ. Simulation of fracture healing in the tibia: mechanoregulation of cell activity using a lattice modeling approach. Journal of Orthopaedic Research. 2011;29(10):1496-1503.
[12] Lacroix D, Prendergast PJ. A mechano-regulation model for tissue differentiation during fracture healing: analysis of gap size and loading. Journal of Biomechanics. 2002;35(9):1163–1171.
[13] Mehboob A, Mehboob H, Kim J, Chang SH, Tarlochan F. Influence of initial biomechanical environment provided by fibrous composite intramedullary nails on bone fracture healing. Composite Structures. 2017;175:123–134.
[14] Ong WH, Chiu WK, Russ M, Chiu ZK. Integrating sensing elements on external fixators for healing assessment of fractured femur. Structural Control and Health Monitoring. 2016;23(12):1388–1404.
[15] Sternick, MB, Dallacosta D, Bento DA, Reis ML. Relação entre rigidez de fixador externo e quantidade de pinos: análise computacional por elementos finitos. Revista Brasileira de Ortopedia. 2012;47(5):646–50.

Journal of Computation and Artificial Intelligence in Mechanics and Biomechanics ISSN 2184-8971
Volume 1, Issue 3, Page 64-70, 2021

Cupula response to otoconia debris in the semicircular canal

Carla F. Santos [1,4], J. Belinha [1,2], Fernanda Gentil [3], Marco Parente [1,4], Renato Natal Jorge [1,4]

[1] *INEGI, Institute of Mechanical Engineering and Industrial Management, Rua Dr. Roberto Frias, Porto, Portugal.*
[2] *School of Engineering, Polytechnic of Porto, (ISEP), Porto, Portugal*
[3] *Clínica ORL-Dr. Eurico Almeida, Widex, Escola Superior de Saúde – I.P.Porto, Porto,Portugal*
[4] *FEUP, Faculty of Engineering of the University of Porto, Rua Dr. Roberto Frias, Porto, Portugal*

Abstract
The vertigo symptoms are commonly related with inner ear diseases and it affects 20%-30% of the world population, and its prevalence increases with age. In this work, a three-dimensional computational model of the semicircular canal of the vestibular system, containing the fluids which promote the body balance, was used. The smoothed-particle hydrodynamics method was the computational process used to simulate the fluid behaviour, in which the elements are represented by particles and have constant mass. The other vestibular components were discretized using the finite element method. The movement performed to endolymph/cupula interaction analysis was reproduced in the simulation through the acquisition of the displacement field based on image analysis. The results obtained with the frames of the video recorded during the process is the appropriate method to simulate the real moves, due to the analysis of the region of interest located near the inner ear. The data obtained from the video acquisition were the input in the simulation with the semicircular model. The principal stress cupular response allowed to understand the interaction of the vestibular structures during a vertigo episode, and the influence of the otoconia in the cupula displacement. This model is the first step to improve the vestibular rehabilitation and the quality of life of patients suffering from vertigo.

***DOI**: 10.5281/zenodo.5710398*

Article Info

Keywords
Finite element method
Meshless methods
Biomechanics
Inner Ear
Vestibular System

Article History
Received: 22/01/2021
Revised: 26/03/2021
Accepted: 11/05/2021

1. Introduction

The main sensory component of the vestibular system is the cupula, located in the semicircular canal (SCC). This structure combined with the macula in the vestibule, comprise the human balance system, which is fulfilled by a fluid called endolymph. The vestibular system, placed in the inner ear, coordinate the gait and body balance function, associated with visual and proprioceptive systems. The vestibular system sends signals primarily to the neural structures that control eye movements, and to the muscles that contributes to keep upright position. Our movements consist of rotations and translations, which are processed in cupula and macula respectively [1]. The macula is a gel layer membrane that contains calcium carbonate crystals called otoconia and have substantially more mass than the cupula. The mass of the otolithic membrane causes the maculae to be sensitive to gravity and linear acceleration. When the otoconia debris is detached from the macula and lost in the SCC, it will influence the endolymph flow and consequently the cupula oscillatory movements will change. This will be translated in an electrical signal distinct from the one that occurs when just the endolymph influences the cupula movement, which will lead do vertigo. According to the body movement performed, a specific electrical signal is expected, however the otoconia in the SCC will change this information and it will not pair with the muscle signal, which will lead to mismatch information in the brain, translating in a vertigo episode. It will lead to a perception of spinning motion, an impression of displacement of the environment to the individual or an intensive sensation of rotation inside the head [2]. The otoconia influence in cupula displacement is not fully understood, which combined with the incapacitate condition of a vertiginous syndrome, turn this an issue of utmost importance regarding a biomechanics point of view.

There are several disorders affecting the vestibular system, most of them lead to vertiginous syndrome, which is the most common symptom in older people. Since vertigo episodes lead to a false sense of rotation, it is important to avoid that kind of symptoms, which in severe cases could cause a fall [3], [4]. Falls are the second leading cause of accidental or unintentional injury deaths worldwide, according to World Health Organization [5]. The vestibular system research

Corresponding Author:
Carla F. Santos
fsantos.carla@gmail.com

could be a partner in prevention strategies development to reduce or avoid the risk of fall. The main treatment applied in the vertigo symptoms caused by otoconia in the SCC is the vestibular rehabilitation procedure, which consists in a set of personalized programed exercises, known as the otoconia repositioning manoeuvres [6]. After the diagnosis, where the affected canal is defined, the suitable manoeuvre is selected. The procedure integrated few evolutions since the manoeuvres creation during the 80's [7], [8]. Some rehabilitation protocols include limitations of movements, until some days after the procedure, which causes anxiety to several patients [9]. Furthermore, the vestibular rehabilitation fails in a certain amount of cases.

The present work goes further than others existing in the literature on obtain a personalized movement of the manoeuvres performed and used it combined with a computational model. This allow to study the cupular movement with less costs compared to other methods (as animal models [10], [11]) as a first step towards a personalized medicine tool, as we could evaluate which movement achieve faster results in the patient, restoring the otoconia back to the vestibule. The aim of the present work is to simulate and analyse the influence of lost otoconia in the cupula activity using computational models, with the last goal of improve quality of life of patients suffering from vertigo, through improved rehabilitation procedures.

2. Methodology

2.1. Geometrical model and properties

The 3D model of the SCC was developed with finite element method (FEM) and composed of three main parts (Fig. 1); a small shell ring that represents one SCC, particles that represent the endolymph fluid inside (simulated with smoothed particle hydrodynamics (SPH)) and the cupula. A mesh with 4478 elements was used to simulate the endolymph as a convergence analysis was performed in the previous SCC model [12]. The model represents the vestibular membrane of the SCC and it is defined as rigid body. In table 1, can be found the properties of the model, as described in the literature for the components of the vestibular system. The model dimensions were defined according the human vestibular system. An otoconia particle is also modelled and included in the SCC, sized 0.15 mm.

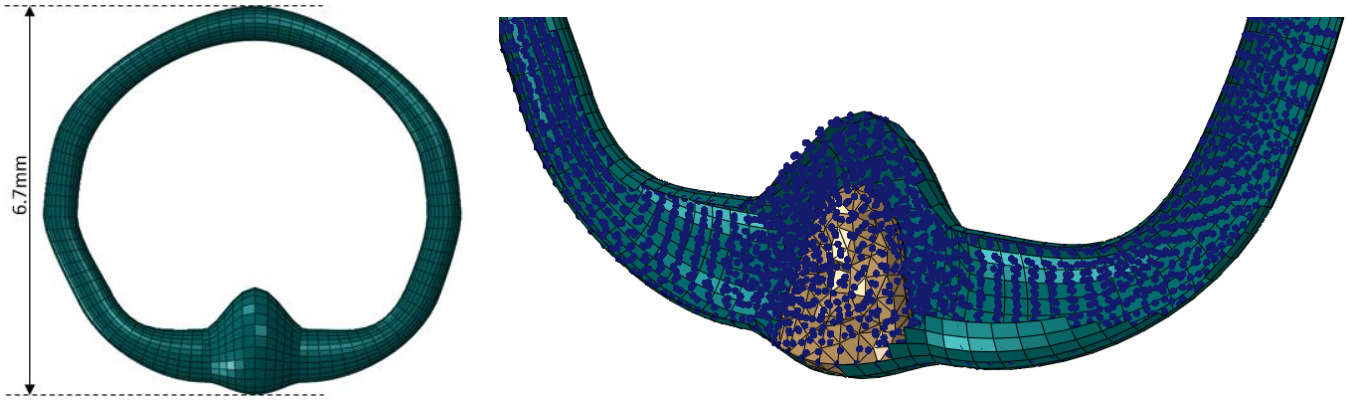

Fig.1 - Semicircular canal with endolymph particles (blue) and the cupula (orange).

Table 1: Properties used in the model [13].

	Young's Modulus (Pa)	Poisson's ratio	Density (kg/m3)	Viscosity (Pa.s)	Element type
Fluid	-	-	$1.0x10^{-3}$	$4.8x10^{-3}$	PC3D
Cupula	5.0	0.49	$1.0x10^{-3}$		C3D4
Membrane	13.7	0.3	$1.85x10^{6}$	-	S4R
Otoconia	6.6	0.45	$3.0x10^{-9}$		C3D4

2.2. Numerical method and boundary conditions

FEM is one of the most common discrete numerical tool used to solve complex problems, such as domains with irregular geometries or structures built with materials showing a non-linear behaviour, which are common features in

biological systems such as the vestibular system. This method is widely used in some scientific fields, including several biological researches to reproduce human systems, due to its great flexibility and efficiency, since cellular level [14] to organs [15] or fully body models [16]. Combined with a constitutive equation, FEM allows the analysis of displacements, stresses and strains, among other measurements [17]. Achieve reliable results without use animal's models in the research performed is another advantage of FEM models.

The SPH method used to simulate the endolymph fluid is a meshless method that works by dividing a continuous field into a set of discrete sample points, with a defined spatial distance, over which their properties are "smoothed" by a kernel function. This approximation is based on the following two steps: the kernel approximation and the particle approximation [18]. The result of the first step is the following quantity function:

$$f(x) = \int_N f(x')W(x - x', h)dx' \tag{1}$$

Where x is any point in the support domain (*N*), and W(x-x',h) is a smoothing kernel function. The influence area of the smoothing function W(x-x',h) is defined by the smoothing length (h), which can be fixed in space and time. The SPH potential was obtaining by assigning to each particle its own smoothing length (variation with time), which can lead to an automatic adaptation of the simulation resolution depending on the domain conditions [18]. W(x) and f(x) as demonstrated below lead to equation 1. The three dimensional position vector x, is the root of integral representation of a function used in SPH:

$$f(x) = \int_N f(x')\delta(x - x')dx' \tag{2}$$

Where $\delta(x - x')$ represents the Dirac delta function given by

$$\delta(x - x') = \begin{cases} 1 & x = x' \\ 0 & x \neq x' \end{cases} \tag{3}$$

If the delta function of equation 3 is replaced in the equation 2 by the smoothing function $W(x - x', h)$, it is possible to obtain the equation 1. The particle approximation plays an important role within the SPH method. The mass of a particle is defined by the relation of density and volume ($m = V\rho$). Thus, the approximation function for a particle i can be represented by the following equation, being the infinitesimal volume dx' in the above equations replaced by the finite volume of the particle j. Where the ρ_j in the density of each particle in the domain N and m_j is the mass of each particle.

$$f(x_i) = \sum_{j=1}^{N} \frac{m_j}{\rho_j} f(x_j)\, W(x_i)\, W(x_i - x_j, h) \tag{4}$$

The boundary conditions imposed in the model include the general contact between the fluid, the membrane and the cupula. The otoconia contact with all the structures is also defined. The gravitational force is imposed to act as a real environment, and finally the angular movement to reproduce the head movement detailed in next sub-section.

The software used to build the model of the vestibular system with finite elements is ABAQUS [19]. This software is one of the most well-known and robust computational frameworks developed for finite element analysis, mainly used for solid models but also successfully used to study biological models [20], [21].

2.3. Video acquisition of the manoeuvres

The movement performed by the audiologist expert during the rehabilitation process will be numerically obtained through video image acquisition. The data retrieved from the video frames, recorded during the therapy, will be used to identify and define analytically the spatial position along time of the interest region located near the inner ear.

A small blue object placed over the ear, in this case a blue bottle cap, was used to trace the head displacement in the sagittal plan by video acquisition. Each point in Fig. 2 represent a step along time during the movement performed. The imposed movements in the SCC model are represented in Fig. 2. The Fig 2(a) corresponds to a benchmark square shape example of the method developed for the present work. The Fig. 2(b) was obtained when the blue bottle cap was placed

in the outer ear, and a flexion extension neck move was performed. The algorithm was able to choose the bluish pixels of the video, as it selects 30 frames per second of the video to identify the coordinates in the plane of the bluish pixel (by a RGB analysis) and save all the data sequentially to trace the displacement of the object in the sagittal plan, which was used as an input in the computational model of the SCC. There are two limitations in the present method, one is that the physician should guarantee that there isn't any other blue area in the frames captured in order to not bias the result and the other is the inability to obtain three-dimensional data.

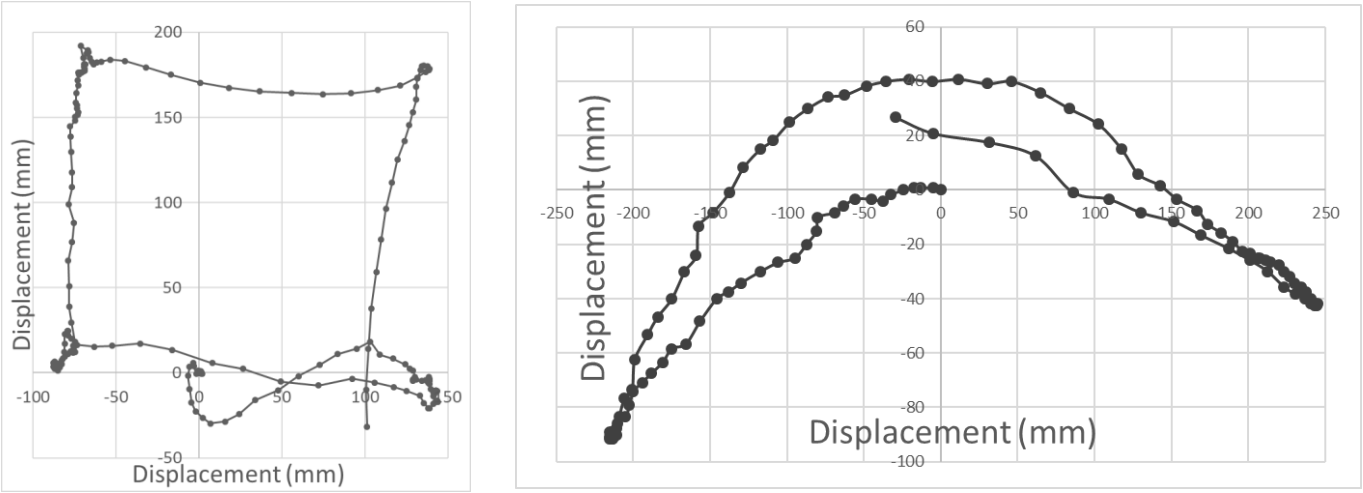

(a) (b)

Fig.2 - Object displacement in sagittal plane obtained with the frames of video acquisition. (a) benchmark, square shape, (b) flexion-extension neck movement.

The two axis correspond to the axial and sagittal planes. The first displacement obtained (Fig. 2(a)) was used in the SCC without otoconia, to notice the fluid flow inside the canal and also the cupula endolymph interaction. The displacement corresponding to a human physiologic motion (Fig. 2(b)) was simulated with the otoconia inside the canal. The results obtained inside the canal, the fluid flow and the otoconia path are shown in the next section.

3. Results

The displacement obtained in the two movements was used as an input in the model of the SCC in two distinct simulations. The square shape movement (Fig 2(a)) was imposed as a boundary condition in the SCC with the cupula and fluid, while the flexion extension neck movement (Fig 2(b)) pretend to simulate a realistic condition with an otoconia inside the canal.

The interaction of the fluid particles with the cupula in the square shape simulation was obtained as expected, and the fluid flow along time was also perceived as could be analysed in Fig.3(a). The results obtained in this benchmark example intends to be a qualitative analysis of the endolymph flow inside the canal and the cupula/fluid interaction under an imposed movement. Fig. 3(a) shows the velocity (magnitude) of the fluid near da cupula during the first horizontal 150 mm section of Fig 2(a), where it is possible to observe an increase in the fluid velocity in the first five steps and then the fluid velocity decline as a change in the direction of the movement occurs. The cupula velocity also increased when the fluid interacts with it as consequence of the experimental displacement input as expected.

In the second simulation, using the displacement of Fig 2(b) as an input, the otoconia pathway inside the canal was obtained and presented in Fig. 3(b). The colour bar legend represents the path evolution along time, the bluish pixel is the initial location of the otoconia at the beginning of the simulation and the yellowish is the final location after the imposed displacement representing the flexion extension neck movement.

Under these results, placing a small blue object near the patient's ear during the manoeuvres will allow to obtain the real movement performed during rehabilitation. When applied to this model, it will allow analysing the interaction of the SCC components. This is an effective and effortless way to obtain the movement performed without disturb the clinical practice. This outcome will improve the rehabilitation since a personalized set of exercises could be prescribed and adapted at each session.

The movement obtained will be applied to this model, it will allow to analyse the interaction of the SCC components, mainly the otoconia path inside the canal. To analyse the cupula behaviour during the flexion extension movement with an otoconia inside the canal, the maximum stress in two nodes in the cupula was obtained (Fig. 4). The nodes A and B

where the stress data were obtained are detailed in Fig. 3(b). The max principal stress (MPa) shown in Fig. 4 corresponds to the node A (red) and node B (blue). The stress result obtained in the two nodes shows the cupula oscillation along the simulation with an amplitude increase in the stress values as the otoconia is closer to the cupula, which proves the influence of the otoconia in the cupula signal transduction. In order to support this argument, a conversion from mechanical energy to electrical energy, as an electrical impulse, should be performed, with the purpose of accurately evaluate the difference between both cases, since it is the brain's input signal regarding the body balance position that triggers dizziness symptoms.

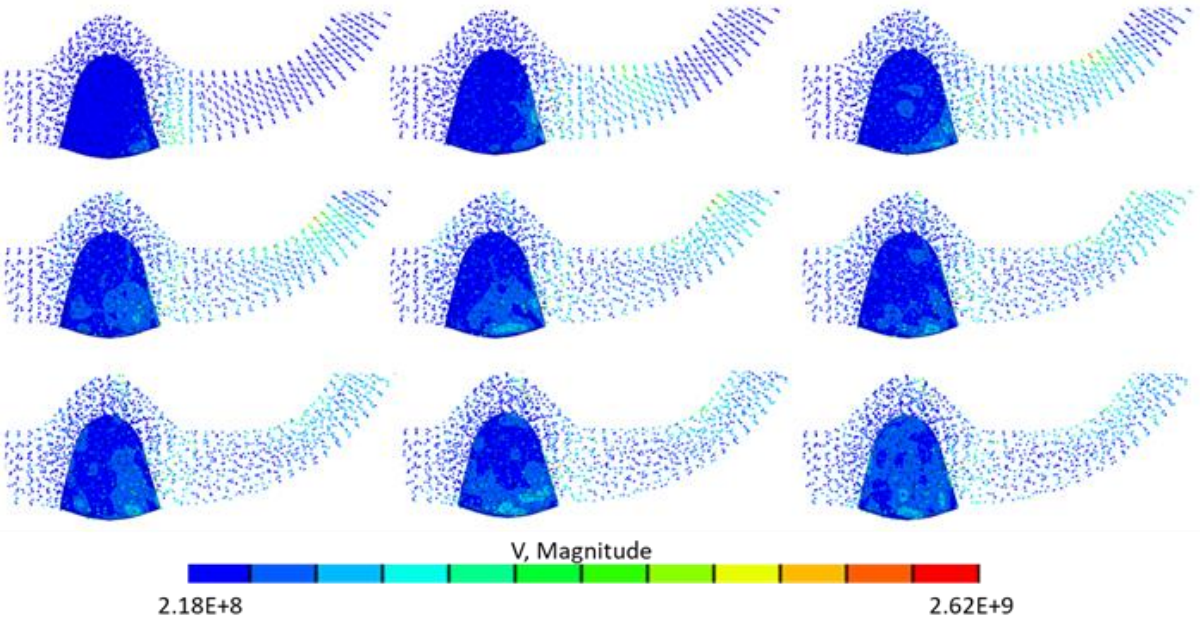

(a)

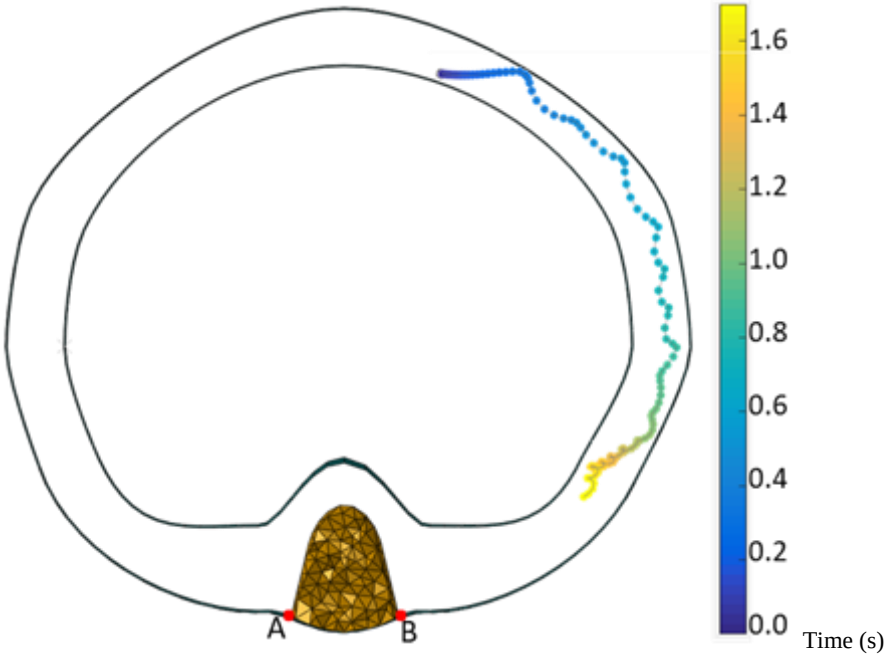

(b)

Fig.3 – (a) Fluid flow (velocity) evolution with the square shape input displacement along time. (b) Otoconia pathway inside the canal along time with the flexion-extension neck movement.

4. Discussion

The model used is the first step to the creation of a complex finite element model of the vestibular system, with all the components. The final model will be built using images from Magnetic Resonance Imaging (MRI), this will help to obtain a more realistic model, which allow to get better results. The results obtained with the frames of the video recorded during the process will be the most appropriate method to simulate the real moves, due to the analysis of the region of interest located near the inner ear. The displacement of the particles inside the shell ring that represent one SCC is similar to the expected and follows the ring moves, as the experimental results obtained in controlled environment of the work of Obrist et al [22], which study a canalithiasis condition as the present work. So this method seems appropriated to simulate the rehabilitation manoeuvres. The results will allow to understand the behaviour of the vestibular structures during the rehabilitation process. Regarding the numerical methods, the SPH fluid particle simulation seems to be the most suitable method for this case, apart from the relevance of explore this methodology combined with FEM.

Obtaining the electrical signals from the mechanical stimulus obtained in FEM simulations could open a new research branch to develop new technologies to be applied in vestibular implants. The computational models allow an infinite hypothesis evaluation without using animal models.

After discovering the right cause of the vertigo in specific individual person it is important to start as soon as possible the rehabilitation process. Although rehabilitation process can be influenced by external factors, which can lead to some less effective results, this method is the most used currently. Understand better the biomechanics of the vestibular system is the first stage to could prepare different kind of simulations with the model. The development of one tool that can help audiology experts in the treatments that they use daily is an important step in that scientific field and can contribute to the fast evolution of the patient.

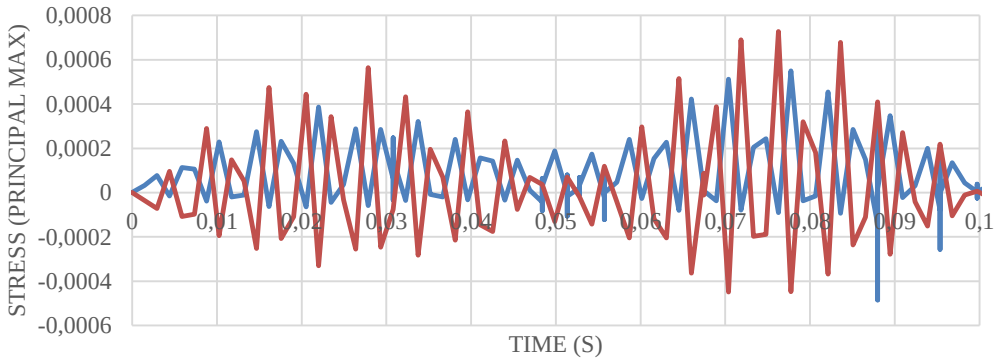

Fig.4 – Maximum Principal Stress of the two nodes in the cupula.

Acknowledgements and Funding

The authors acknowledge the funding by "Ministério da Ciência, Tecnologia e Ensino Superior —Fundação para a Ciência e a Tecnologia , Portugal and POCH —Programa Operacional Capital Humano, comparticipado pelo Fundo Social Europeu e por fundos nacionais do MCTES" under research grants SFRH/BD/108292/2015 and by project funding MIT- EXPL/ISF/0084/2017. Additionally, the authors gratefully acknowledge the funding of Project NORTE-01-0145-FEDER-000022 —SciTech —Science and Technology for Competitive and Sustainable Industries, cofinanced by Programa Operacional Regional do Norte (NORTE2020), through Fundo Europeu de Desenvolvimento Regional (FEDER).

References

[1] S. J. Herdman, *Vestibular rehabilitation.*, vol. 26, no. 1. 2013.

[2] J. Taylor and H. P. Goodkin, "Dizziness and vertigo in the adolescent.," *Otolaryngol. Clin. North Am.*, vol. 44, no. 2, pp. 309–21, vii–viii, Apr. 2011, doi: 10.1016/j.otc.2011.01.004.

[3] M. Karatas, "Central Vertigo and Dizziness," *Neurologist*, vol. 14, no. 6, pp. 355–364, Nov. 2008, doi: 10.1097/NRL.0b013e31817533a3.

[4] C. F. Santos, J. Belinha, F. Gentil, M. Parente, and R. N. Jorge, "The free vibrations analysis of the cupula in the inner ear using a natural neighbor meshless method," *Eng. Anal. Bound. Elem.*, vol. 92, pp. 50–63, Jul. 2018, doi:

10.1016/J.ENGANABOUND.2018.01.002.
[5] World Health Organization, "Falls," 2018. Accessed: Aug. 16, 2018. [Online]. Available: http://www.who.int/news-room/fact-sheets/detail/falls.
[6] B. a Alsalaheen *et al.*, "Vestibular rehabilitation for dizziness and balance disorders after concussion.," *J. Neurol. Phys. Ther.*, vol. 34, no. 2, pp. 87–93, Jun. 2010, doi: 10.1097/NPT.0b013e3181dde568.
[7] J. M. Epley, "New dimensions of benign paroxysmal positional vertigo.," *Otolaryngol. Head Neck Surg. (1979).*, vol. 88, no. 5, pp. 599–605, Accessed: Nov. 23, 2018. [Online]. Available: http://www.ncbi.nlm.nih.gov/pubmed/7443266.
[8] J. M. Epley, "Positional vertigo related to semicircular canalithiasis.," *Otolaryngol. Head. Neck Surg.*, vol. 112, no. 1, pp. 154–61, Jan. 1995, [Online]. Available: http://www.ncbi.nlm.nih.gov/pubmed/7816450.
[9] J. Burzynski, S. Sulway, and J. A. Rutka, "Vestibular Rehabilitation: Review of Indications, Treatments, Advances, and Limitations," *Curr. Otorhinolaryngol. Rep.*, vol. 5, no. 3, pp. 160–166, Sep. 2017, doi: 10.1007/s40136-017-0157-1.
[10] A. Rüsch and U. Thurm, "Cupula displacement, hair bundle deflection, and physiological responses in the transparent semicircular canal of young eel," *Pflügers Arch. Eur. J. Physiol.*, vol. 413, no. 5, pp. 533–545, 1989, doi: 10.1007/BF00594186.
[11] R. D. Rabbitt, K. D. Breneman, C. King, A. M. Yamauchi, R. Boyle, and S. M. Highstein, "Dynamic displacement of normal and detached semicircular canal cupula," *JARO - J. Assoc. Res. Otolaryngol.*, vol. 10, no. 4, pp. 497–509, Dec. 2009, doi: 10.1007/s10162-009-0174-y.
[12] C. F. Santos, J. Belinha, F. Gentil, M. Parente, and R. N. Jorge, "An alternative 3D numerical method to study the biomechanical behaviour of the human inner ear semicircular canal.," *Acta Bioeng. Biomech.*, vol. 19, no. 1, pp. 3–15, 2017, Accessed: Oct. 23, 2017. [Online]. Available: http://www.ncbi.nlm.nih.gov/pubmed/28552920.
[13] C. Wu, C. Hua, L. Yang, P. Dai, T. Zhang, and K. Wang, "Dynamic analysis of fluid-structure interaction of endolymph and cupula in the lateral semicircular canal of inner ear," *J. Hydrodyn. Ser. B*, vol. 23, no. 6, pp. 777–783, Dec. 2011, doi: 10.1016/S1001-6058(10)60176-X.
[14] A. Boccaccio, A. Ballini, C. Pappalettere, D. Tullo, S. Cantore, and A. Desiate, "Finite element method (FEM), mechanobiology and biomimetic scaffolds in bone tissue engineering," *International Journal of Biological Sciences*, vol. 7, no. 1. Ivyspring International Publisher, pp. 112–132, 2011, doi: 10.7150/ijbs.7.112.
[15] R. Werner, J. Ehrhardt, R. Schmidt, and H. Handels, "Patient-specific finite element modeling of respiratory lung motion using 4D CT image data," *Med. Phys.*, vol. 36, no. 5, pp. 1500–1511, Apr. 2009, doi: 10.1118/1.3101820.
[16] D. Schwartz, B. Guleyupoglu, B. Koya, J. D. Stitzel, and F. S. Gayzik, "Development of a Computationally Efficient Full Human Body Finite Element Model," *Traffic Inj. Prev.*, vol. 16, no. sup1, pp. S49–S56, Jun. 2015, doi: 10.1080/15389588.2015.1021418.
[17] J. N. (Junuthula N. Reddy, *An introduction to the finite element method*. McGraw-Hill Higher Education, 2006.
[18] G. R. Liu and M. B. Liu, *Smoothed Particle Hydrodynamics*. WORLD SCIENTIFIC, 2003.
[19] M. Smith, "ABAQUS/Standard User's Manual, Version 6.9." Dassault Systèmes Simulia Corp, 2009, Accessed: Sep. 15, 2020. [Online]. Available: https://www.research.manchester.ac.uk/portal/en/publications/abaqusstandard-users-manual-version-69(0b112d0e-5eba-4b7f-9768-cfe1d818872e).html.
[20] K. Berdich *et al.*, "Finite element analysis of the transfer of sound in the myringosclerotic ear," *Comput. Methods Biomech. Biomed. Engin.*, vol. 19, no. 3, pp. 248–256, Feb. 2016, doi: 10.1080/10255842.2015.1010526.
[21] F. Gentil *et al.*, "Effects of the fibers distribution in the human eardrum: A biomechanical study," *J. Biomech.*, vol. 49, no. 9, pp. 1518–1523, Jun. 2016, doi: 10.1016/j.jbiomech.2016.03.030.
[22] D. Obrist, S. Hegemann, D. Kronenberg, O. Häuselmann, and T. Rösgen, "In vitro model of a semicircular canal: design and validation of the model and its use for the study of canalithiasis.," *J. Biomech.*, vol. 43, no. 6, pp. 1208–14, Apr. 2010, doi: 10.1016/j.jbiomech.2009.11.027.

Journal of Computation and Artificial Intelligence in Mechanics and Biomechanics ISSN 2184-8971
Volume 1, Issue 3, Page 71-80, 2021

The computational simulation and impact analysis of the rib bones

Dilki Dias [1], Jorge Belinha [2]

[1] *Faculty of Engineering, University of Porto, up201909597@fe.up.pt, Porto, Portugal*
[2] *Department of Mechanical Engineering, School of Engineering, Polytechnic of Porto, job@isep.ipp.pt, Porto, Portugal*

Abstract
Ribs have crucial functions in the human body, most importantly provide protection to the vital inner organs such as heart and lungs. Yet the rib fractures are the most common bone fractures in blunt force accidents. Therefore, understanding more about the impact responses of the ribs is necessary. This study analyses the impact responses of the first and third ribs using the finite element method. A CT image of the thorax was used to obtain the geometric model of the individual ribs. Models with 3D tetrahedral meshes were created and appropriate boundary conditions were imposed. The material of the bone was considered elastic, isotropic and homogenous. The elasto-static analysis was conducted using FEMAS academic software. Distinct variable fields, such as displacement, von Mises equivalent stress, first and third principal stresses, were studied when a constant magnitude load is applied to three different points on the ribs, assuming two distinct directions. Displacement and stress variations along the inner and outer borders of each rib were analysed. Obtained results suggest that a load applied to the lateral region of the bone is the most acute case, showing the highest displacement and stress values. Thus, such findings, indicate the location of a possible fracture (or catastrophic damage) in both rib bones.

***DOI**: 10.5281/zenodo.5710422*

Article Info

Keywords
Rib bones
Finite Element Method
Load impact analysis
Biomechanics

Article History
Received: 13/11/2020
Revised: 28/03/2021
Accepted: 05/05/2021

1 Introduction

Rib cage provides protection and support to the human body. The heart and lungs are protected by the ribs. Hence rib fractures can lead to injuries in the internal organs causing severe situations. Rib fractures are regular in automobile crashes and fallings, and represent the most common bone fracture occurring in 10–20% of all blunt trauma patients [1]. However, uncomplicated single rib fractures can be managed easily but multiple rib fractures may result in a pneumothorax, a life-threatening emergency [2].

Humans have 24 ribs, in 12 pair. Each rib is a curved, flattened bone that contributes to the wall of the thorax. The superior ribs (1 to 3) are relatively protected by the scapula, clavicle, and soft tissue [3]. Ribs have 3 major regions namely posterior, anterior and lateral. The anterior extremity is connected to costal cartilages of the sternum and the posterior extremity is connected to the respective thoracic vertebra. The ribs are constituted by cortical and trabecular bones [4].

In the field of biomechanics, post- mortem human subject (PMHS) tests, anthropomorphic test devices (ATDs) and computational simulations have been applied over the years to analyse the structural variations of the ribs during impact. With recent developments in computational methods, such as finite element methods, meshless methods and other discrete numerical techniques, the use of computational models to simulate real scenarios has been increased. However, the accuracy of the computational methods mainly depends on the model quality, geometry and mechanical properties. Finite Element Method (FEM) is the most popular discrete technique used in modern biomechanical analysis. Automotive crash simulations and injury analyses are performed with different testing methods, mostly with full thoraces models, full-body models or lab models. When analysing the impact responses on rib bones, generally thoracic models or individual ribs have been used. However small-scale refined models are believed to represent an accurate geometric model since large scale models usually present an oversimplified geometry [5][6][7]. Past studies suggest that cortical bone thickness and cross-sectional geometry are important factors of rib impact response analysis, which can be achieved through FE models [8].

Corresponding Author:
Jorge Belinha
job@isep.ipp.pt

This study aims to analyse the impact responses of the first and third rib when loads are applied to different regions of the rib as well as in distinct directions. The Finite Element and Meshless Analysis Software (FEMAS) academic software (cmech.webs.com) was used to perform the structural analysis of the ribs.

2 Methodology and Materials

This study utilizes models of first and third ribs which were obtained from anonymized CT images of the thorax, which allows to acquire an accurate geometric model. CT image was converted into 3D solid meshes with tetrahedral elements for each separated rib.

A first rib model with 1531 nodes and 5417 elements and third rib model with 1253 nodes and 3815 elements were obtained. The human ribs consist of highly vascular cancellous bone, enclosed in a thin layer of cortical bone. Previous studies propose that human rib bones are anisotropic and viscoelastic [9][10]. However, since the cortical and cancellous bones have different material properties, their contribution to the whole rib properties are different as well. As Ayagara, 2019 explains, the cortical bone can be modelled as isotropic [11]. In another study conducted by Li et al., 2010, it was found that in human ribs, changes of trabecular bone properties has negligible influence on rib responses compared to cortical bone [12]. Hence, in this study, the rib models consist of a cortical bone shell with variable thickness, which is assumed to be elastic, isotropic and homogenous. The average mechanical properties were adopted from literature analysis ([7] [12] [13] [14]), as Young's modulus to be 13.9GPa and Poisson's ratio to be 0.3. Finally, the computational mechanical analysis was conducted on the two models using FEMAS academic software.

In each rib, three points were chosen, and a determined force was applied from two directions making 6 load cases, to analyse the loading impacts on the ribs. The analysed load cases consist of three loads applied in the Oz direction (F1, F2, F3) and another three loads applied in the Ox direction, (F4, F5, F6), as figures 1(b) and figure 2(b) show. All the applied loads possess the same absolute magnitude of 500N. As depicted in figure 1 a) and 2 a), both extremities of the ribs are fixed where the rib connects with the costal cartilage and thoracic vertebra, constraining the degrees of freedom off all nodes indicated in white. To analyse the regional variations of stresses and displacement, inner and outer border of the ribs, as indicated in figure 1 c) and figure 2 c), were selected.

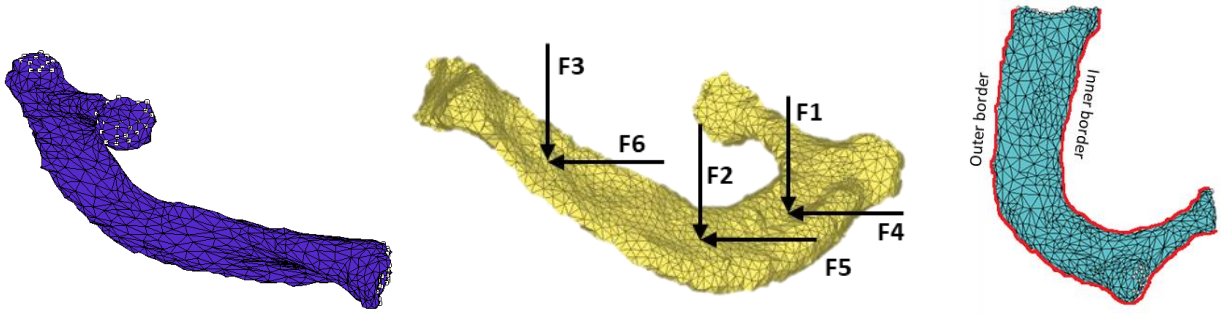

(a) (b) (c)

Fig. 1 - First Rib bone (a) Boundary conditions (b) Applied load cases (c) Analysed regions

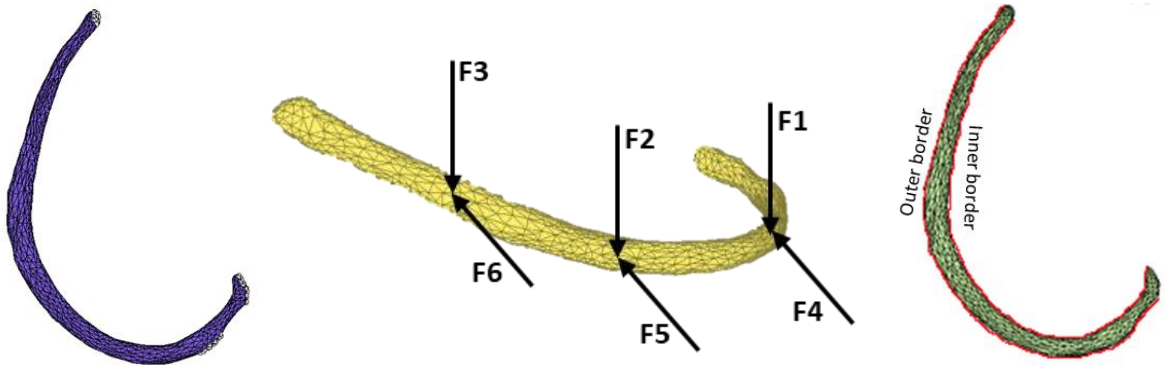

(a) (b) (c)

Fig. 2 - Third Rib bone (a) Boundary conditions (b) Applied load cases (c) Analysed regions.

3 Results

The elasto-static analysis was conducted on each rib using constant strain tetrahedral elements. Absolute displacement, Von Mises stress, first and third principal stresses were analysed in both ribs with 6 different load cases.

Figures 3 and 4 present the absolute displacements of the first and third ribs respectively, with their maximum and minimum values. The first rib reaches a maximum displacement of 0.55mm when F2 is applied (negative Oz-direction), 0.055mm is the lowest displacement reached by F6 (positive Ox-direction). The highest value of the third rib is 7.9 mm when the F2 is applied and 0.73 mm minimum displacement was reached when F4 is applied.

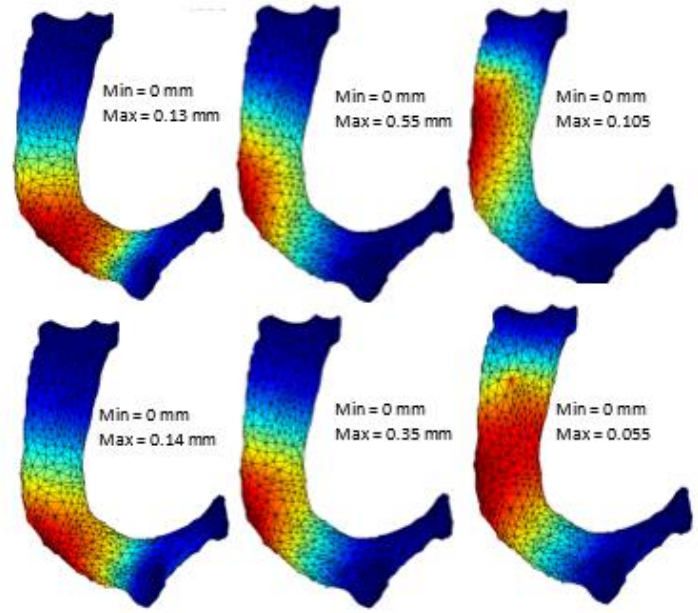

Fig. 3 - Displacement colour maps of the first rib with each load case from F1 to F6, respectively

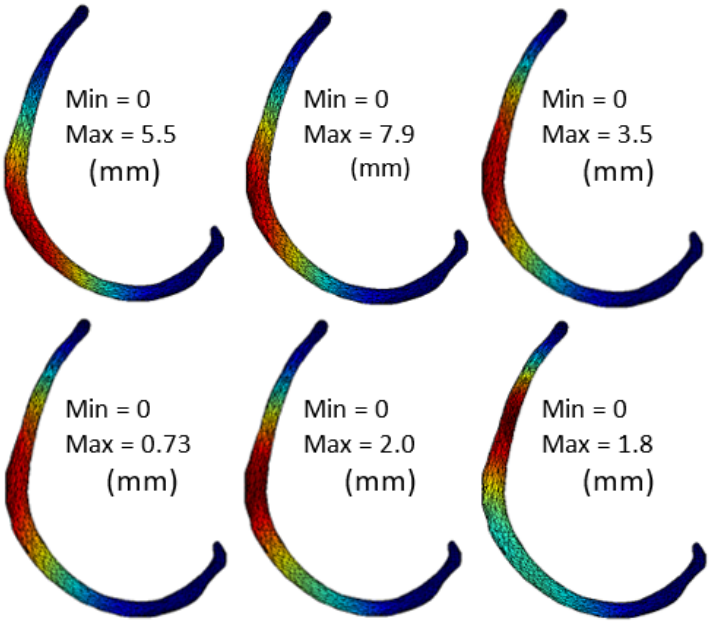

Fig. 4 - Displacement colour maps of the third rib with each load case from F1 to F6, respectively.

In von Mises failure theory, it is considered that energy absorbed during the distortion is responsible for failure [15]. In this theory, if the stress exceeds the yield stress, failure occurs. Figures 5 and 6 present the von Mises stress from the first and third rib, respectively. A maximum of 52 MPa von Mises stress value was reached when the F1 is applied.

Minimum stress was obtained in the F3 with 30MPa. In the third rib, comparably high stresses can be observed with the maximum value of 270 MPa in F2 and the lowest value of 52 MPa when the F4 is applied. In most cases, the highest stress is concentrated on the rib where it connects with the rib cage (anterior and posterior articular facets).

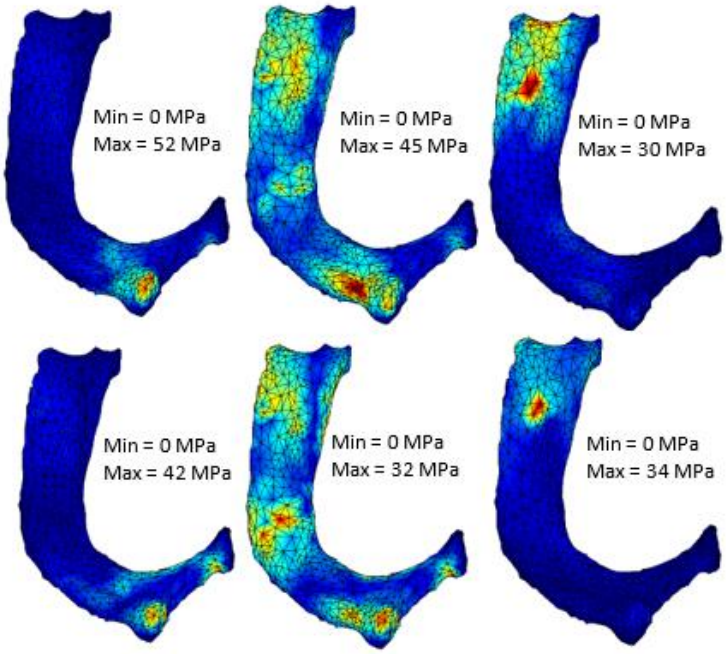

Fig. 5 - Von Mises stresses of the first rib with each load case from F1 to F6, respectively.

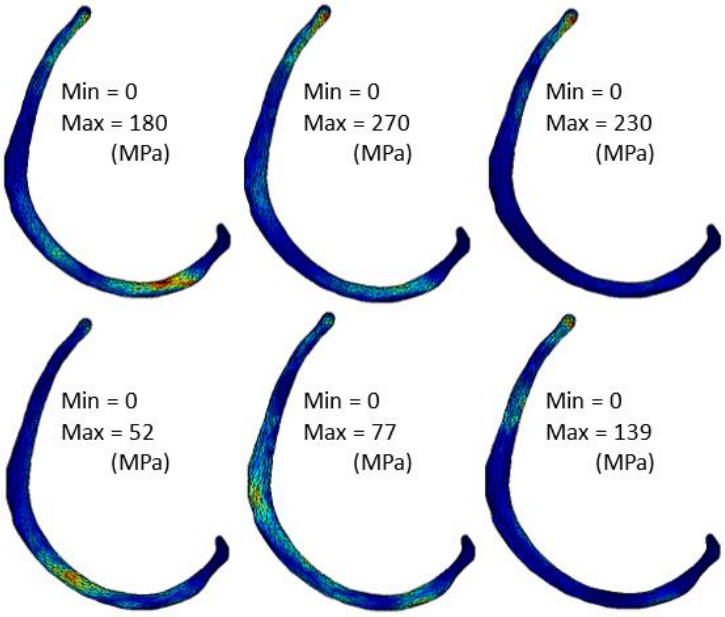

Fig. 6 - Von Mises stresses of the third rib with each load case from F1 to F6, respectively.

Principal stresses in a complex 3D load case indicate the maximum and minimum normal stresses that a point reaches in a particular plane. The first principal stress indicates the highest value in an element and the lowest value is considered as the third principal stress. Figures 7 and 8 represent the first principal stresses and figures 9 and 10 present the third principal stresses. The first principal stress of the first rib (Figure 7), the F1 causes the highest maximum principal stress (71 MPa) and the lowest maximum stress were caused by the F6 (-4 MPa). The highest minimum principal stress of the

first rib is noted to be -59MPa (Compressive Stress) from F4 and the lowest minimum stress is 7 MPa from F6, as figure 9 shows.

Figure 8 includes the first principal stress of the third rib from load case F1 to F6. In the third rib, the highest both maximum and minimum stresses were obtained when the F2 applied, values being 370 MPa and -255 MPa, respectively. And the lowest both maximum and minimum stress were observed in the F4 with -13 MPa and 8 MPa, respectively, as in figure 10.

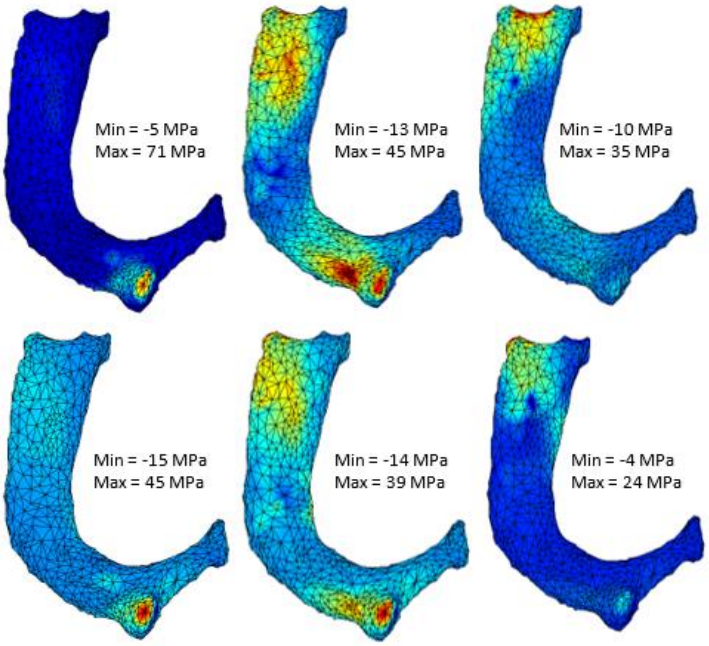

Fig. 7 - First principal stress of the first rib with each load case from F1 to F6, respectively.

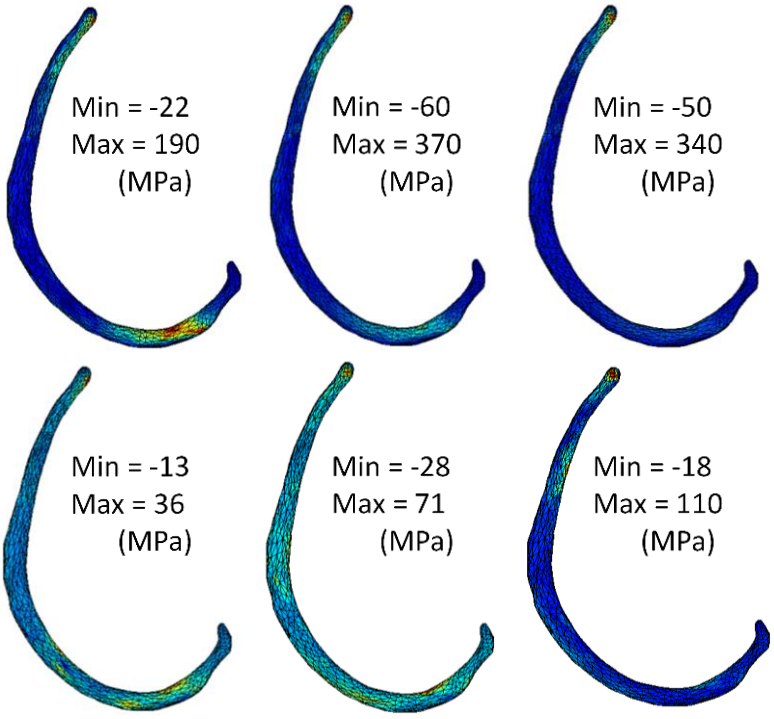

Fig. 8 - First principal stress of the third rib with each load case from F1 to F6, respectively.

4 Discussion

This study was conducted to analyse the load impact on the first and third rib bone using the finite element method. Displacement, von Mises stress and principal stresses were obtained for each rib when 6 different load cases were applied. Analysing the results from the obtained figures, the third rib suffers considerably higher stresses and displacements than the first rib when enforced the same magnitude of loads. This can be expected since the first rib has a higher cross-sectional area compared with the third rib. In both ribs, the lateral section of the rib displaces more than the posterior or anterior ends in all load cases, mostly concentrated on the load applied point. The first rib seems to be having higher von Mises stress, first and third principal stresses in the tubercle articular facet of the rib. The third rib has its higher stresses in the sternal extremity.

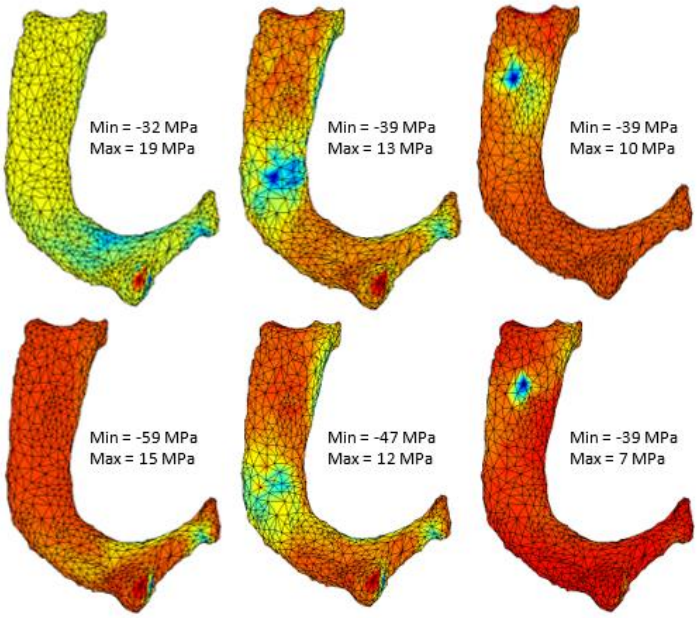

Fig. 9 - Third principle stress of the first rib with each load case from F1 to F6, respectively.

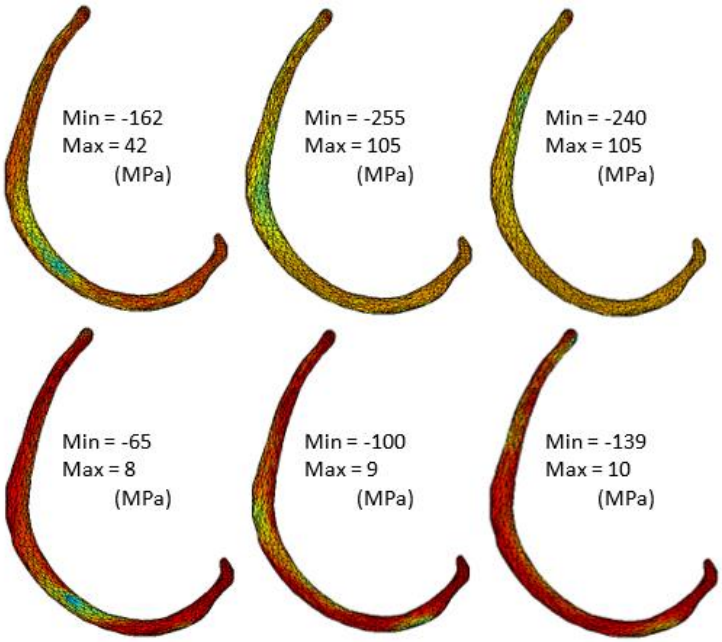

Fig. 10 - Third principal stress of the third rib with each load case from F1 to F6, respectively

Furthermore, observing colour maps for the first rib, the F2 load is noted to impose the highest displacement and highest von Mises and first principal stress are inflicted by F1 and F2 load cases, F4 and F5 impose the highest third principal stresses. In the third rib, the highest displacement, highest von Mises stress, maximum first and third stresses were obtained when F2 applied. To obtain a clearer idea of the impact change of each load along the ribs, displacements and stresses were analysed along the points of both interior and exterior borders of each rib and graphed against the border length.

As seen in figures 11 and 12, the inner border of the first rib is less displaced, but allows higher von Mises, first and third principal stresses compared with the exterior border. In addition, it can be observed that in both borders the F2 and F5 load cases cause maximum displacement and higher stresses while F6 imposes the lowest values. F1, F3 and F4 load cases have occasional higher values mostly where the loads are applied. The load cases F1 and F2 are noted to have a higher displacement in both the inner and outer borders of the third rib. Higher von Mises, first and third principal stresses are caused by F1, F2 and F3 load cases. Moreover, F4, F5 and F6 loads have a relatively lower impact on the third rib, as presented in figure 13 and 14.

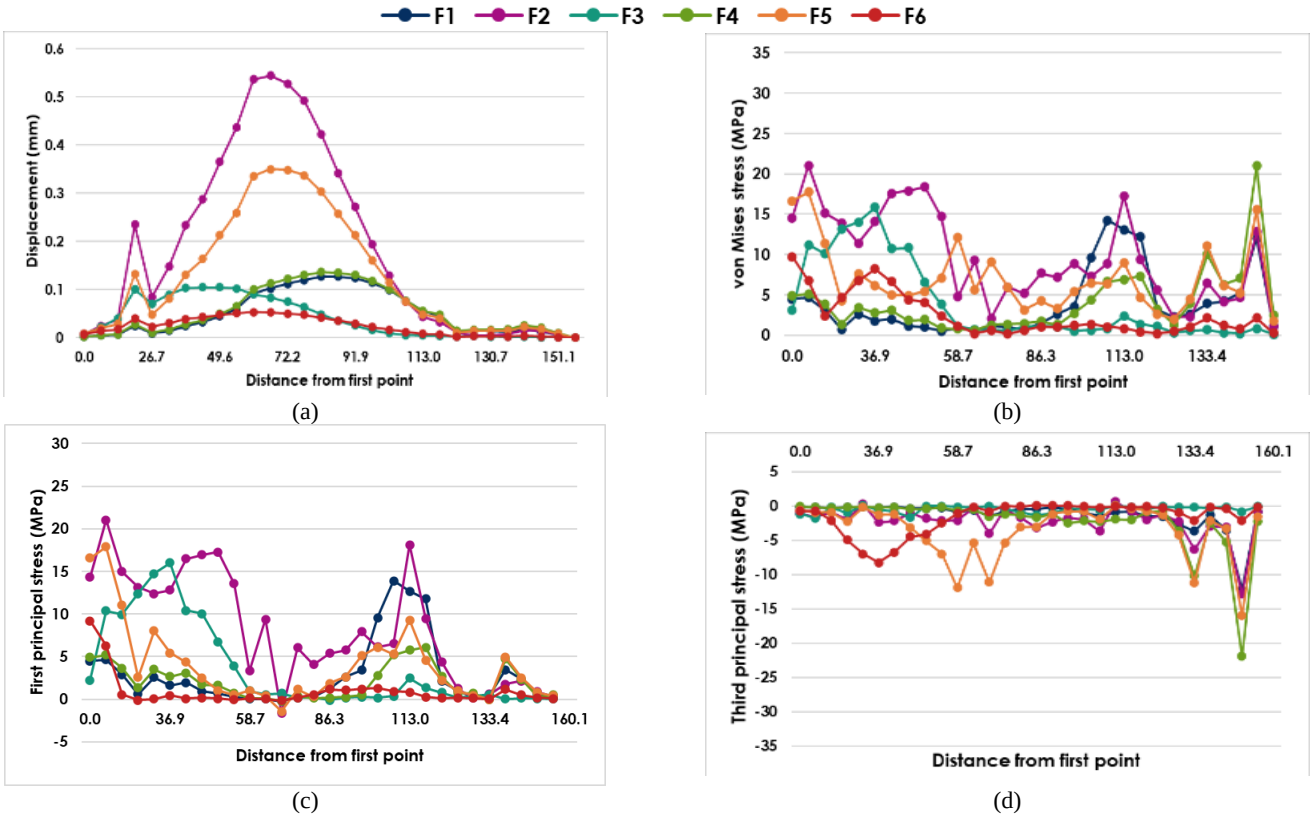

Fig. 11 - Structural analysis of the outer region of the first rib (a) Displacement (b) von Mises stress (c) First principal stress (d) Third principal stress, graphed against the distance from the first point.

5 Conclusion

Results were studied by enforcing the same magnitude load on 3 different points with two directions on each rib bone. In the first rib, the severer load was found to be F1 having maximum von Mises stress and first principal stress. Furthermore, F2 load case is having relatively higher stresses. The highest displacement was caused when a load applied to the lateral region of the rib (F2 and F5). Loads applied to the anterior region are noted to cause the least impact.

In the third rib, unlike the first rib, the severe load case depends more on the applied direction rather than the position. It was noted that loads applied from Ox-direction had a higher impact on bone than the Oz-direction. The most acute load case was applied to the lateral position of the rib, F2. Meanwhile, in both ribs, the outer border suffers higher displacement and higher stresses than on the inner border.

There are a few limitations regarding the model and properties used in this study. Constant material properties were used throughout the rib but in reality, the Young's modulus might vary in the lateral, posterior and anterior regions of the rib [16].

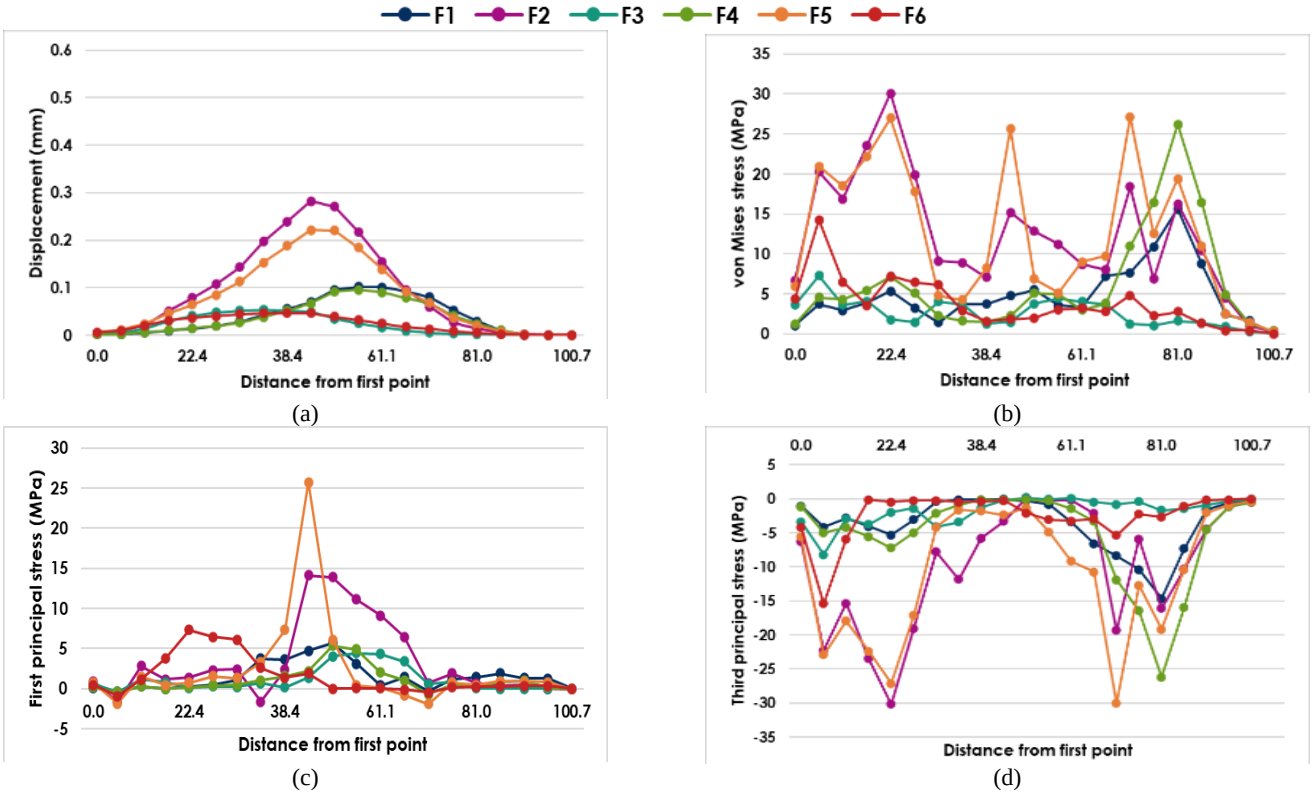

Fig. 12 - Structural analysis of the inner region of the first rib (a) Displacement (b) von Mises stress (c) First principal stress (d) Third principal stress, graphed against the distance from the first point.

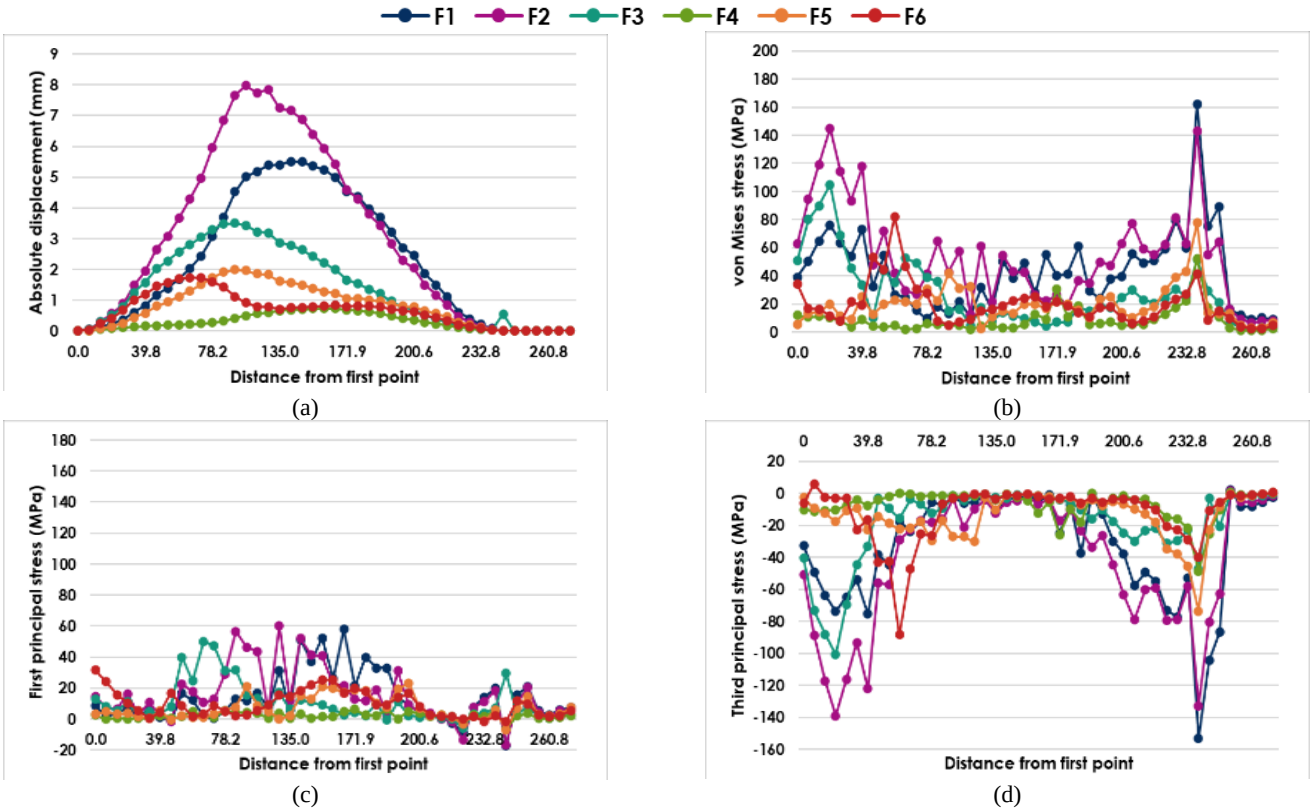

Fig. 13 - Structural analysis of the outer region of the third rib (a) Displacement (b) von Mises stress (c) First principal stress (d) Third principal stress, graphed against the distance from the first point.

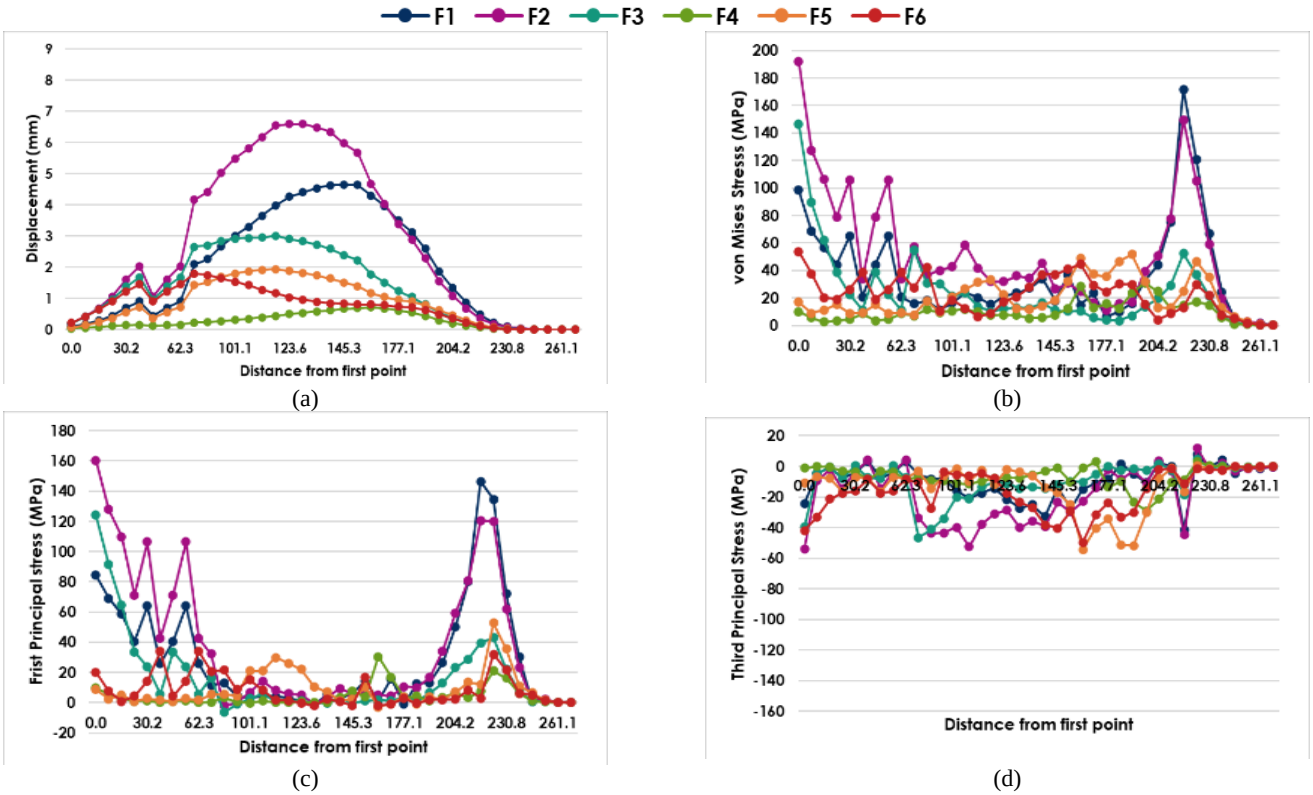

Fig. 14 - Structural analysis of the inner region of the third rib (a) Displacement (b) von Mises stress (c) First principal stress (d) Third principal stress, graphed against the distance from the first point.

Soft tissues and internal organs also affect the impact responses of the ribs, hence ribs have complex 3-dimensional boundary conditions, which are complex to simulate. The bone mechanical properties were assumed to be elastic, homogenous and isotropic. Despite these limitations, this study has shown that it is possible to use open source software to perform computational analysis of impact testing of individual ribs.

Acknowledgements

The authors truly acknowledge the funding provided by Ministério da Ciência, Tecnologia e Ensino Superior - Fundação para a Ciência e a Tecnologia (Portugal), under funding provided by LAETA: project UIDB/50022/2020.

References

[1] C. Liebsch, T. Seiffert, M. Vlcek, M. Beer, M. Huber-Lang, and H. J. Wilke, "Patterns of serial rib fractures after blunt chest trauma: An analysis of 380 cases," *PLoS One*, vol. 14, no. 12, 2019, doi: 10.1371/journal.pone.0224105.

[2] "Rib Fracture and Pneumothorax Complication - Sports Injuries, treatment and performance information." https://www.sportsmd.com/sports-injuries/chest-rib-injuries/rib-fracture-pneumothorax-complication/ (accessed Aug. 20, 2020).

[3] V. Magesh and S. Sundar, "Finite element analysis of human rib bone and implant design," Accessed: Aug. 22, 2020. [Online]. Available: www.jchps.com.

[4] "The Ribs - Human Anatomy." https://theodora.com/anatomy/the_ribs.html (accessed Aug. 22, 2020).

[5] Z. Li, M. W. Kindig, D. Subit, and R. W. Kent, "Influence of mesh density, cortical thickness and material properties on human rib fracture prediction," *Med. Eng. Phys.*, vol. 32, no. 9, pp. 998–1008, Nov. 2010, doi: 10.1016/j.medengphy.2010.06.015.

[6] B. Michelle Ann Schafman, J. Bolte, A. Amanda Agnew, and C.-A. Rebecca Dupaix, "Dynamic Structural Properties of Human Ribs in Frontal."

[7] D. Subit, E. Del Pozo De Dios, J. Velázquez-Ameijide, C. Arregui-Dalmases, and J. Crandall, "Tensile material properties of human rib cortical bone under quasi-static and dynamic failure loading and influence of the bone microstucture on failure characteristics," 2013.

[8] S. A. Holcombe, Y. Kang, B. A. Derstine, S. C. Wang, and A. M. Agnew, "Regional maps of rib cortical bone thickness and cross- sectional geometry," *J. Anat.*, vol. 235, no. 5, pp. 883–891, Nov. 2019, doi: 10.1111/joa.13045.

[9] W. T. Dempster and R. T. Liddicoat, "Compact bone as a non- isotropic material," *Am. J. Anat.*, vol. 91, no. 3, pp. 331–362, 1952, doi: 10.1002/aja.1000910302.
[10] R. S. Lakes, J. L. Katz, and S. S. Sternstein, "Viscoelastic properties of wet cortical bone-I. Torsional and biaxial studies," *J. Biomech.*, vol. 12, no. 9, pp. 657–678, Jan. 1979, doi: 10.1016/0021-9290(79)90016-2.
[11] A. R. Ayagara, "Characterization of human ribs under dynamic impact loads: Finite Element simulations and experimental validation." Accessed: Mar. 27, 2021. [Online]. Available: https://hal.archives-ouvertes.fr/tel-02568503.
[12] Z. Yumin, "Evaluation in vivo chez l'enfant du comportement mecanique du thorax." Accessed: Sep. 02, 2020. [Online]. Available: https://tel.archives-ouvertes.fr/tel-01015789.
[13] A. Robb Kemper, S. M. Duma, C. H. Clay Gabler, and J. D. Stitzel, "Material Properties of Human Rib Cortical Bone From Dynamic Tension Coupon Testing," 2005.
[14] A. Kemper, C. McNally, C. Pullins, L. Freeman, S. Duma, and S. Rouhana, "The biomechanics of human ribs: Material and structural properties from dynamic tension and bending tests," *Stapp Car Crash J.*, vol. 51, pp. 235–273, 2007.
[15] L. Srinath, *Advanced mechanics of solids*, 3rd ed. New Delhi: Tata McGraw-Hill, 2009.
[16] M. F. Stitzel JD, Cormier JM, Barretta JT, Kennedy EA, Smith EP, Rath AL, Duma SM, "Defining regional variation in the material properties of human rib cortical bone and its effect on fracture prediction.," *Stapp Car Crash J.*, 2003.

Journal of Computation and Artificial Intelligence in Mechanics and Biomechanics ISSN 2184-8971
Volume 1, Issue 3, Page 81-91, 2021

Development of a DoE with a new electrospinning system for cartilage tissue engineering

Silva E. [1], Semitela A. [2], Marques P.A.A.P. [3], Completo A. [4]

[1] *eduardasilva@ua.pt; Universidade de Aveiro; Aveiro; Portugal*
[2] *angela.semitela@ua.pt; Universidade de Aveiro; Aveiro; Portugal*
[3] *paulam@ua.pt; Universidade de Aveiro; Aveiro; Portugal*
[4] *completo@ua.pt;Universidade de Aveiro; Aveiro; Portugal*

Abstract
Electrospinning is currently one of the most used techniques to produce fibrous synthetic tissues such as cartilage and bone. To replicate cartilage tissue engineering functionality, one of the most important characteristics is the alignment of the resulting fibre meshes in a three-dimensional (3D) fashion. Here, a newly developed electrospinning collector system is tested in order to understand how the process parameters affected the obtained fibre meshes topography. For that, a polymer consisting of PCL/Gelatin was electrospun using the electrostatic potential to create a fibre mesh. A Design of the Experiments (DoE) approach was implemented, to determine whether the variation of the main process parameters led to significant effects on the mesh dimensional characteristics. The process parameters analysed were the velocity of the collecting bands, the linear velocity of the fibre deposition table and the flow rate. The analysed mesh characteristics were the fibre diameter, the distance between the fibres and pore size. The effect of each of the three factors was statistically analysed using ANOVA, as well as the interaction between them. Complementary an ANOVA linear regression approach was developed to predict the distance between the fibres. This statistical regression was then compared with a predictive theoretical model and with the experimental results. The results obtained indicate the presence of interactions between the three process parameters analysed. The three process parameters showed statistical significance in the distance between the fibres, however, the velocity of the deposition table was the process parameter that presented the highest effect.

***DOI**: 10.5281/zenodo.5710429*

Article Info

Keywords
Electrospinning
Nanofiber alignment
Biomechanics
Tissue Engineering
Design of Experiments
Biofabrication
ANOVA

Article History
Received: *27/01/2021*
Revised: *05/04/2021*
Accepted: *14/05/2021*

1. Introduction

In the current days, one of the biggest challenges in cartilage tissue engineering (TE) is the difficulty to mimic the biomechanical environment of cartilage's native tissue [1-8]. So far, various biofabrication techniques have been used [1, 9-15], in which it was possible to develop artificial cartilage with similar biochemical properties to the native tissue. The main limitation remains on the fact that the artificial cartilage developed does not recapitulate the fibril zonal variances the native cartilage tissue does [1, 12-15]. The organization of the collagen fibrils through the depth of the cartilage tissue is extremely important and should be replicated in the artificial tissue for it to become mechanically functional [12-14, 16]. This can be achieved using anisotropic fibrous scaffolds since they allow mimicking the extracellular matrix (ECM) structure/organization of native tissues [11-14]. Electrospinning is a process for the development of polymer nanofibres [1, 5-6, 8] using electrostatic potential to create a continuous fiber that can be collected in the form of a mat. This technology has been widely used in the field of TE to produce synthetic tissue, such as cartilage [9-15]. However, it is necessary to find an efficient way to control the alignment of polymeric nanofibres matrices during the electrospinning process in order to mimic the topography of the native cartilage ECM [9-15]. In this study, a recently developed electromechanically electrospinning system [17] was employed on the fabrication of aligned nanofibres mats. This electrospinning platform has the capacity to control the fibre alignment as well as the distance between the aligned fibres and thus the scaffold pore size. The pore size, as the fibre diameter, are important factors affecting tissue regeneration efficiency [11-12]. Thus, an experiment plan (DoE) for the automated electrospinning system was developed in order to understand how the velocity of the collecting bands, the velocity of the deposition table and the flow rate would affect the dimensional characteristics of the resulting nanofibres mats, as the fibre diameter and pore size. Complementary, a mathematical model was developed capable of predicting the dimensional characteristics of the nanofibres mats, and the results compared with the experimental ones.

Corresponding Author:
António Completo
completo@ua.pt

2. Methods and Materials

2.1. Materials

Polymeric solutions of polycaprolactone (PCL; Sigma-Aldrich) and Gelatin from porcine skin (Sigma-Aldrich) were dissolved separately in 2,2,2-trifluoroethanol (TFE; TCI) at a concentration of 10 wt % and mixed in a 60:40 volume ratio, respectively, to be used throughout the entire experimental procedure. Previous studies have reported the use of that PCL blends to produce aligned nanofibres and to recreate cartilage's composition [11-12, 18]. PCL is a biodegradable polymer extensively used in TE due to its suitable tensile property and biocompatibility [9-15]. However, this polymer's hydrophobicity and slow biodegradation rate are restraints on its applications. Gelatin is a congener protein of collagen and is a widely utilized biomaterial [10-11]. However, its fast degradation time and its highly hydrophilic surface may not be appropriate as the base material. To overcome the respective limitations of these two materials and take each other's advantages, PCL/gelatin hybrid nanofibrous structures obtained by electrospinning have been successfully developed for biomedical applications [10-11].

2.2. Electrospinning System

A new electrospinning system was used [17] where the PCL solution was placed inside a syringe attached to a pump, which forms the emitter module (+20kV) of the system, as it can be seen in Fig. 1. Besides the emitter module, the system also contains a collecting and deposition module. The collecting module, also shown in Fig. 1, consists of two rotating, metallic bands (Band 1 and Band 2), that attract the electrospun fibres. The result is a fibre mat formed in the gap between the two bands, as shown in Fig. 1, the bands are the only metallic component in the module which are negatively charged (-5kV). The moving deposition table then collects a specific ratio of the resulting mat of fibres. The deposition table moves linearly along the three-axis (XYZ), and rotates around the Z-axis (C), as schematically explained in Fig. 2. The resulting deposited fibres on the table, look like the example also shown in Fig. 2.

A specific software was developed to control the various movements of the modules of the electrospinning system [17]. This software has both a manual and an automatic mode, and it allows to create a routine of steps for the modules of the system to follow, such as the flow rate, the position and the linear velocity of both the collecting bands and the deposition table, and the rotational velocity of the latter. The number of repetition cycles can also be defined by the software.

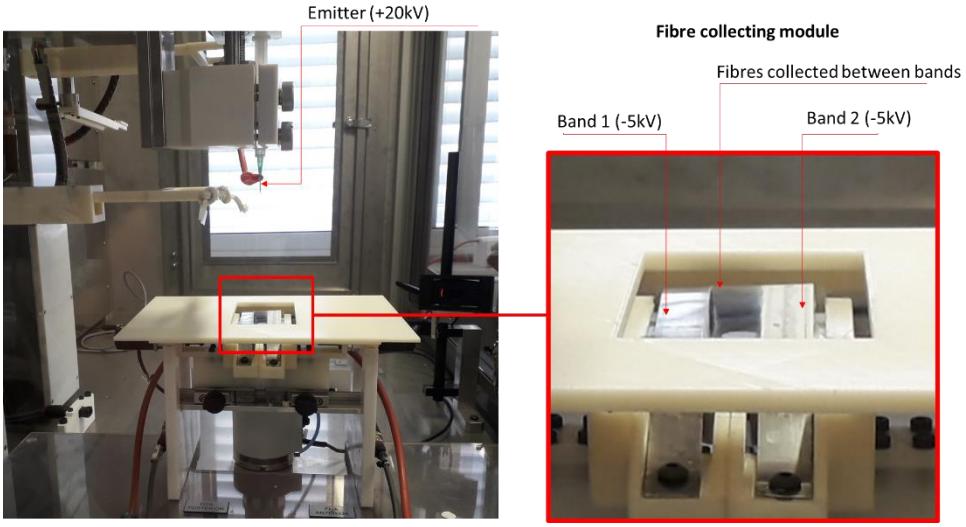

Fig. 1 – Electrospinning setup and its fibre-collecting module.

The experiments (each sample) were conducted with five repetition cycles for each orientation of the deposition table (0º and 90º), this means that, in total, the experimental samples had ten layers of fibres. The resulting meshes were visualized via scanning electron microscopy (SEM, Hitachi TM4000 plus, Japan) at an accelerating voltage of 5 kV. Based on the SEM images, fibre diameter, pore size and distance between the aligned fibres were determined using Image JPro Plus software.

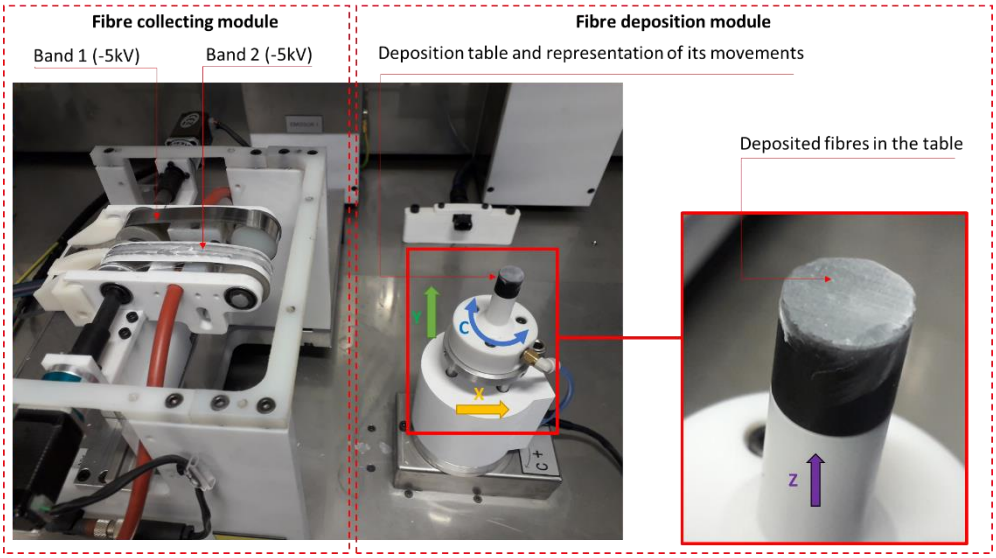

Fig. 2 – Electrospinning setup and its fibre deposition system.

2.3. Design of Experiments (DoE)

Having a better understanding of how the electrospinning equipment's modules work, helps to make a prediction on which factors could have a direct effect on the distance between the fibres and consequently in the mesh porosity. The velocity of the collecting bands (A), as well as the velocity of the deposition table (B), are the two factors that stand out for the ease of control they provide. Moreover, the flow rate (C) is also a defining factor on the distance between the fibres since it controls the amount of fibre that leaves the syringe which are collected by the two bands.

Table 1 – Design of Experiments table.

	Factors			Interactions between factors				Experimental Values		
Experiment	A	B	C	AB	AC	BC	ABC	A (mm/min)	B (mm/min)	C (mL/h)
1	-1	-1	-1	1	1	1	-1	2000	250	2
2	1	-1	-1	-1	-1	1	1	6000	250	2
3	-1	1	-1	-1	1	-1	1	1000	500	2
4	1	1	-1	1	-1	-1	-1	6000	500	2
5	-1	-1	1	1	-1	-1	1	1000	125	3
6	1	-1	1	-1	1	-1	-1	4000	250	3
7	-1	1	1	-1	-1	1	-1	2000	500	3
8	1	1	1	1	1	1	1	6000	500	3
9	-1	-1	-1	1	1	1	-1	1000	500	2
10	1	-1	-1	-1	-1	1	1	5000	500	1,5
11	-1	1	-1	-1	1	-1	1	3000	750	1,5
12	1	1	-1	1	-1	-1	-1	4000	750	1,5
13	-1	-1	1	1	-1	-1	1	2000	500	4
14	1	-1	1	-1	1	-1	-1	4000	500	4
15	-1	1	1	-1	-1	1	-1	3000	750	4
16	1	1	1	1	1	1	1	5000	750	4

The output mesh variables to be evaluated will be the distance between the fibres since the main goal of the present work is to understand how this variable is affected to find an effective way to produce meshes with aligned fibres with controllable spacing between them. The second output variable to be screened is the mesh pore size, which is highly dependent on the previous variable mentioned. Finally, the third output variable will be the diameter of the resulting fibre. The distance between the fibres is the main factor to be analysed because it is highly connected with the size of the pores of the resulting fibre matrix. The pore size is a critical factor for the chondrocytes' migration progress into the scaffold [11-14].

A two-level factorial design was used to generate the DoE. Since there are three factors, 2^3 experiments needed to be conducted; however, to reach more accurate results and to analyse the interaction between elements, replication was used. The full DoE matrix is represented in Table 1, with a total of 16 experiments. The parameter's low and high values were defined based on previous experiments realised in other studies [9-15], such that the difference between the high and low levels would most likely have a statistical impact.

2.4. Theoretical Model

Theoretically analysing the entire process of the electrospinning system is fundamental to have a general idea of the output results, if no outside factors were influencing. Thus, a mathematical function was developed, taking into account the variables of the electrospinning process; flow rate (F), the velocity of the collecting bands (V_{bands}), and velocity of the deposition table (V_{table}) -, to calculate the distance between the fibres deposited in the table.

Consider that the polymer used on the experiment is released from the syringe at a constant velocity, calculated as shown in Eq. (1).

$$V_{fiber} = \frac{F}{\pi \cdot r_{needle}{}^2} \quad \text{[mm/min]} \tag{1}$$

The collecting bands have a width of 12 mm each, as well as the distance between them. Thus, the total width (W) available for the deposition is 36 mm. Considering that the velocity of the collecting bands is zero, the time it takes to deposit a thread of fibre ($t_{deposition}$) can be calculated by Eq. (2).

$$t_{deposition} = \frac{W}{V_{fiber}} \quad \text{[min]} \tag{2}$$

Having the time each segment of fibre takes to be deposited on the collecting bands, it is possible to calculate the distance between the fibres on the collecting bands (S_{bands}) by multiplying the time of deposition with the velocity of the collecting bands, as shown in Eq. (3).

$$S_{bands} = V_{bands} \cdot t_{deposition} \quad \text{[mm]} \tag{3}$$

In order to calculate the distance between the deposited fibres on the deposition table, since its velocity is a parameter that can be controlled, a simple multiplication of the latter Eq. (3) by the time it takes to deposit the fibres on the collecting bands should result in the distance between the fibres on the deposition table – Eq. (4).

$$S_{table} = \frac{S_{bands}}{V_{bands}} \cdot V_{table} \quad \text{[mm]} \tag{4}$$

This theoretical model was tested in Matlab to see if it can predict the behaviour of the resulting distance between the fibres. For an analysis on how each variable affects the result maintaining the other parameters constant, it was conducted a graphical interpretation of the problem, represented in Fig. 3. The graphs show that the velocity of the collecting bands does not have any effect on the distance between the fibres collected by the deposition table. This makes sense since when the fibres are on the collecting bands, the only factor that should affect the distance they will have on the deposition table is the velocity of the latter. The faster the table moves the fewer fibres it collects, thus, the bigger the distance between them.

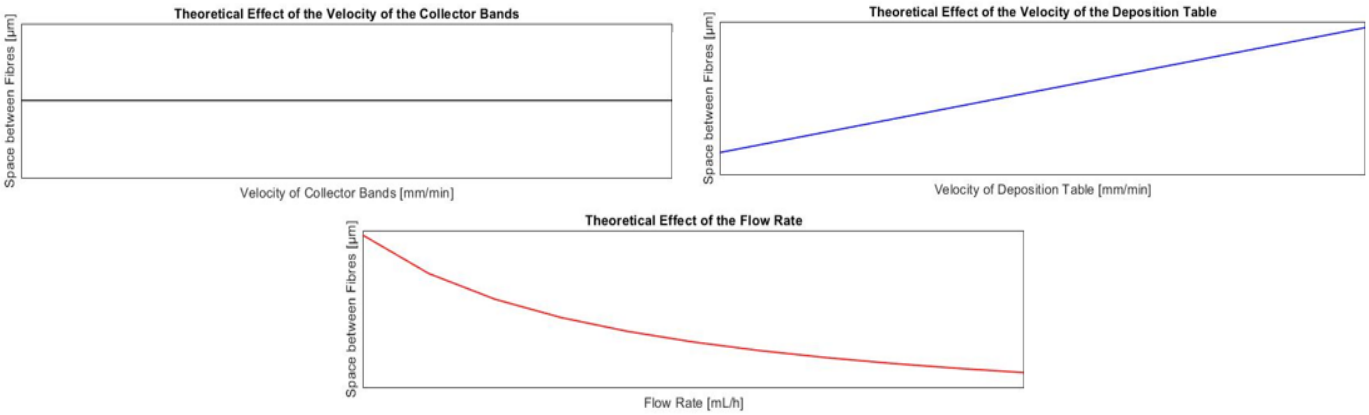

Fig. 1 – Theoretical model's response to input variations (left) and its response to random inputs generated by Matlab (right).

3. Results and Discussion

3.1. Statistical Analysis

Using ImageJ, and after defining the right scale for the SEM image, ten measurements of the distance between the most parallel aligned fibres at 0º and 90º were made (Fig. 4).

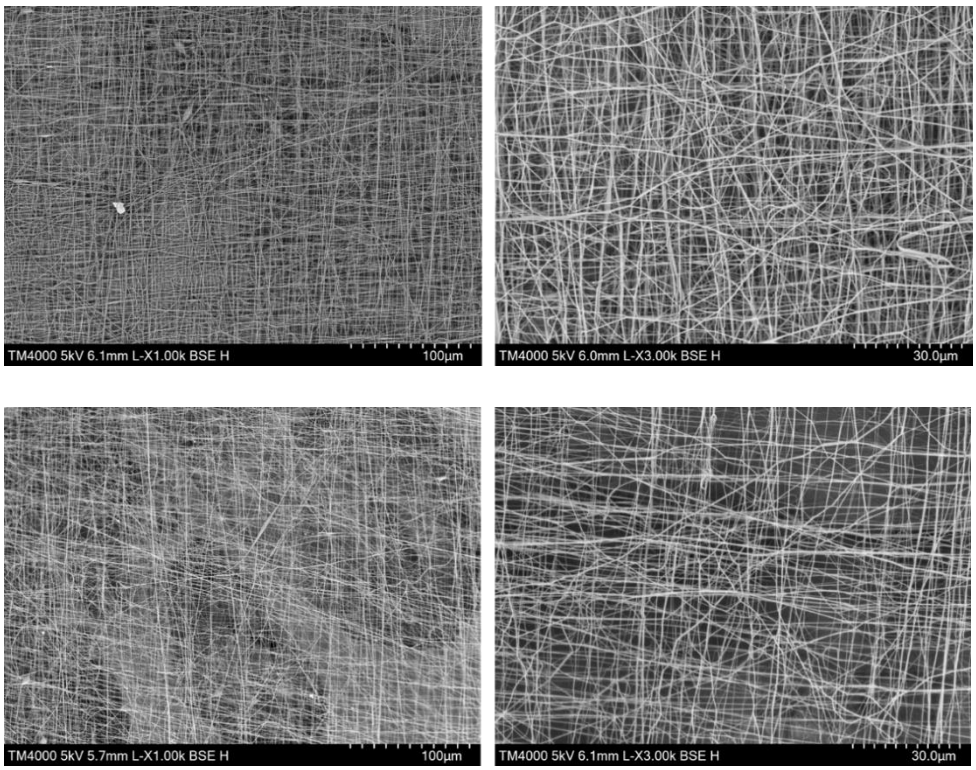

Fig. 4 – Examples of SEM images of two mesh samples: experiment 15 (up) and experiment 2 (down).

With the ten measurements made for each experimental trial, a statistical analysis was conducted using a three-factor ANOVA. Table 2 shows the results for the distance between the aligned fibres. Of all the information presented in the ANOVA table, the primary interest will be focused on "*p-value*", because this is the exact significance level of the factors. If $p<0.05$ then the effect is said to be significant.

Table 2 – ANOVA table for the distance between the aligned fibres (SS- sum-of-squares; df- degrees of freedom; MS- mean squares; F- F ratio).

Factors & Interactions	SS	df	MS	F	p-value
V_{bands} (A)	415,906	5	83,181	3,429	0,007
V_{table} (B)	421,222	3	140,407	5,788	0,001
F (C)	588,885	3	196,295	8,092	0,000
$V_{bands} \cdot V_{table}$ (A x B)	283,062	15	18,871	0,778	0,699
$V_{bands} \cdot F$ (A x C)	1099,347	15	73,290	3,021	0,001
$V_{table} \cdot F$ (B x C)	1125,434	9	125,048	5,155	0,000

Analysing the table presented, it can be concluded that all three independent factors have significance ($p<0.05$) in the resulting distance between the fibres. Moreover, the interactions between the flow rate (F) and the V_{bands}, as well as between V_{table} and the flow rate, also show significance in the results. The next step is to understand precisely how, and how much, the factors, and the interaction between them, influence the results. To do that, the measured values of the distance between the fibres were processed to produce main effect plots and interaction plots, represented in Figs. 5 and 6, respectively.

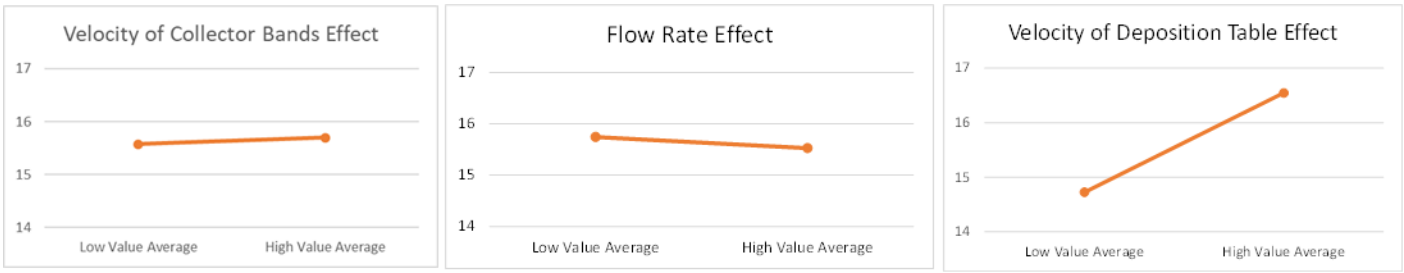

Fig. 5 – Effects of the input parameters on the distance between the aligned fibres

The values presented in Fig. 5 are the means at each level (high/low) under consideration for the parameters, stated in the DoE. Each graph has two points connected by a solid line. The steeper the gradient of the line, the more significant the difference between the two means and, consequently, the higher the influence of the factor. Thus, it can be concluded that the element that has the most impact on the distance between the fibres is the velocity of the deposition table. When increasing the velocity of the deposition table, the distance between the fibres also increases, which was expected. The flow rate has a negative effect, as it can be seen by the slope of the line; when increasing its value, the distance between the fibres will decrease, which was also expected.

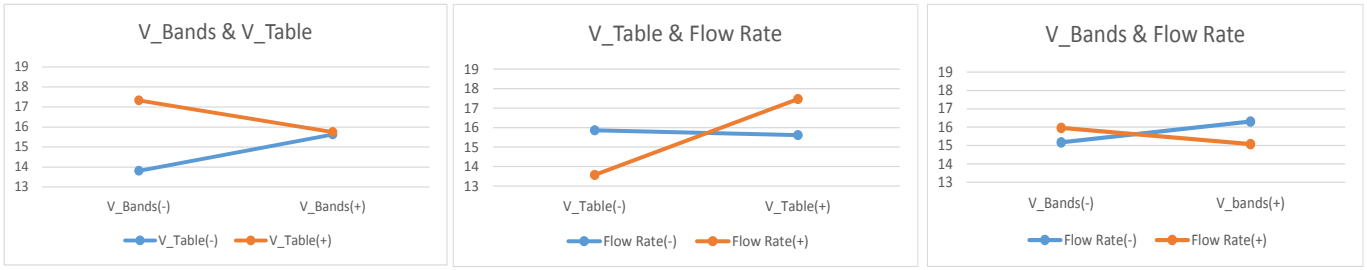

Fig. 6– Interaction plots for the distance between the fibres.

The interaction plots, shown in Fig. 6, give indicators as to how the factors affect the output parameters in combination with each other. The indication is provided by the slope of the 2 lines of each plot, such as the less parallel the lines are, the more likely there is to be a significant interaction between the factors.

Regarding the first interaction plot (V_{bands} and V_{table}), since line V_{table} (+) is, in general, higher than V_{table}(-), it can be concluded that the main effect should be expected in this factor, such that high values of the table's velocity leads to

a higher distance between the fibres. This states that when the factors interact, the dominant factor is the velocity of the deposition table. Even though there is an interaction between the two factors, as the graph proves, the ANOVA table states it is not significant for the results.

There is an interaction between the V_{table} and the flow rate since the lines are not parallel at all. Since the values for the Flow rate (-) are not higher or lower than the values of the Flow rate (+), there is no main effect for flow rate when in combination with the velocity of the deposition table. This is because the velocity of the deposition table shows, in general, a higher impact on the results than the flow rate.

The same analysis was conducted for the fibre diameter. Table 3 contains the results of the ANOVA calculations and it can be concluded that both the velocity of the collecting bands and the flow rate have some significance on the resulting diameter of the fibres. Moreover, both the interactions between the flow rate (F) and the V_{bands}, and the V_{table} and the V_{bands}, also have significance.

Table 3 – ANOVA table for fibre diameter (SS- sum-of-squares; df- degrees of freedom; MS- mean squares; F- F ratio).

Factors & Interactions	SS	df	MS	F	p-value
V_{bands} (A)	0,088	5	0,018	5,574	0,001
V_{table} (B)	0,018	3	0,006	1,881	0,138
F (C)	0,038	3	0,013	3,983	0,010
$V_{bands} \cdot V_{table}$ (A x B)	0,135	15	0,009	2,831	0,001
$V_{bands} \cdot F$ (A x C)	0,131	15	0,009	2,759	0,001
$V_{table} \cdot F$ (B x C)	0,025	9	0,003	0,884	0,543

As it can be seen in Fig. 7, the parameter that has a more significant influence in the fibre diameter is the flow rate ($p<0.05$), as it is the line with the highest slope. The V_{bands} also shows a significant effect on the fibre diameter, increasing the value of the diameter as V_{bands} also increases. The parameter indicating the least amount of influence, and according to ANOVA, not presenting any significance, is the V_{table}.

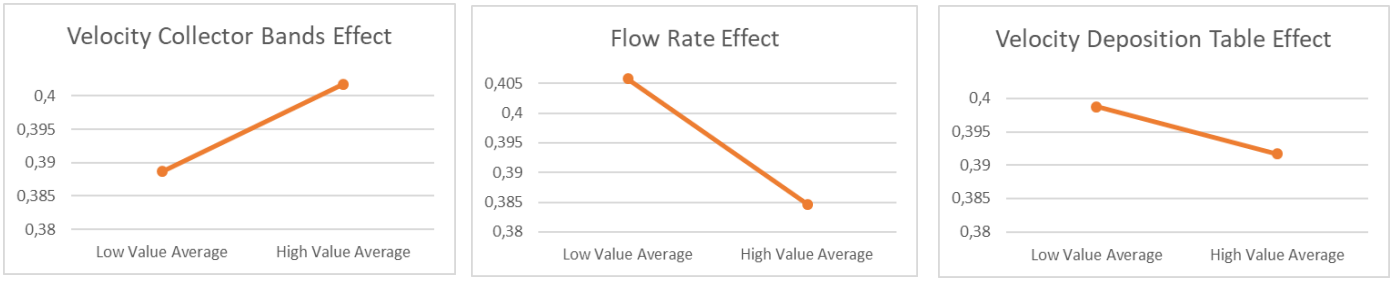

Fig. 7 - Effects of the input parameters on the fibre diameter.

Analysing the interaction plots in Fig. 8, it can be deduced that the flow rate interacts energetically with the velocity of the collecting bands; however, the main effect, when the two parameters interact, is expected to be the V_{bands}.

The lines in the plot of flow rate and V_{table} do not cross each other, which leads to the idea that, if there is an interaction between the two factors, it is very tiny. The ANOVA table shows that there is no significance in the interaction between these two factors, which was expected since, by the time the fibres arrive at the deposition table, the diameter is already defined.

In the plot regarding the interaction between the V_{bands} and V_{table}, the lines come very close to crossing each other, which leads to consider there should be an interaction between the two factors, however, not significant.

The three-factor ANOVA results for the data regarding the pore size are indicated in Table 4. By analysing the data from this table, it can be concluded that, similarly to the results from the distance between the fibres, all the three factors have significance on the results, as well as the interactions between the flow rate and the V_{bands}, and the flow rate and the V_{table}. It was expected that the same factors showed significance since the pore size is highly dependent on the distance between the fibres.

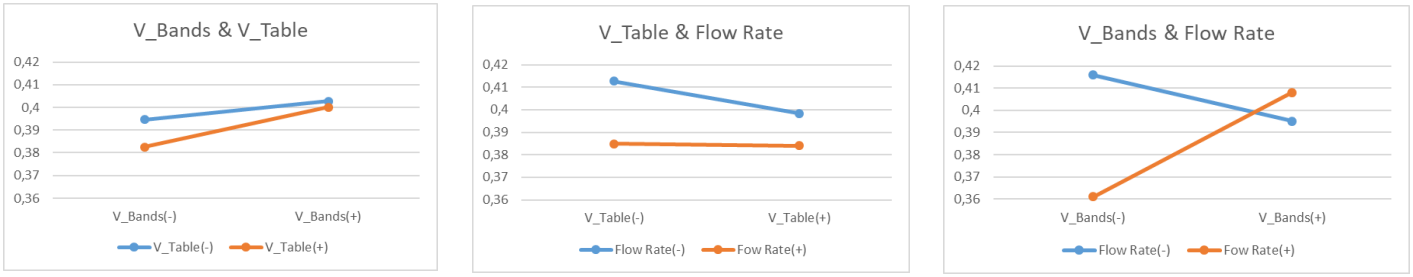

Fig. 8 - Interaction plots for the fibre diameter.

Table 4 – ANOVA table for pore size (SS- sum-of-squares; df- degrees of freedom; MS- mean squares; F- F ratio).

Factors & Interactions	SS	df	MS	F	p-value
V_{bands} (A)	34,051	5	6,810	4,779	0,001
V_{table} (B)	17,758	3	5,719	4,013	0,010
F (C)	29,195	3	9,717	6,818	0,000
$V_{bands} \cdot V_{table}$ (A x B)	6,048	15	0,403	0,283	0,996
$V_{bands} \cdot F$ (A x C)	56,837	15	3,789	2,659	0,002
$V_{table} \cdot F$ (B x C)	32,588	9	3,621	2,541	0,012

As it can be seen in Fig. 9, the parameter that has a more significant influence in the pore size is the velocity of the deposition table, which is in accordance with the results from the effect analysis of the distance between the fibres. The velocity of the bands shows a similar effect on the pore size to the one showed on the distance between the fibres, such that higher values lead to bigger pore sizes and the flow rate shows a positive impact. It should be expected that the parameters behaved similarly to the distance between the fibres, however, that is not the case for the flow rate.

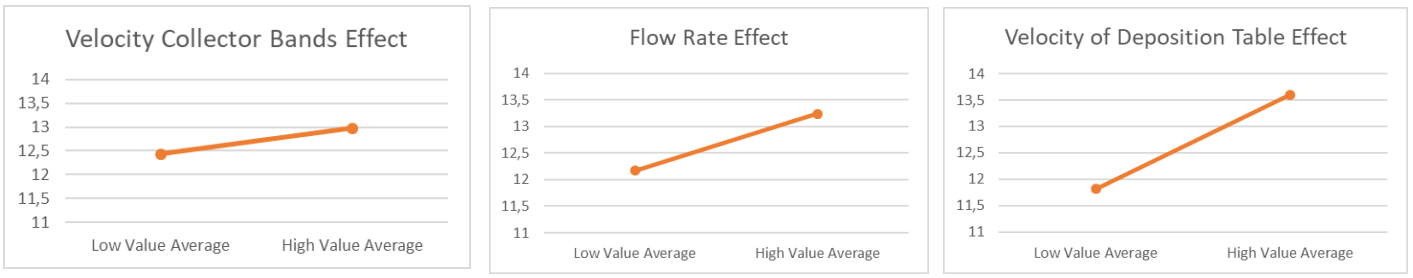

Fig. 9 - Effects of the input parameters on the pore size.

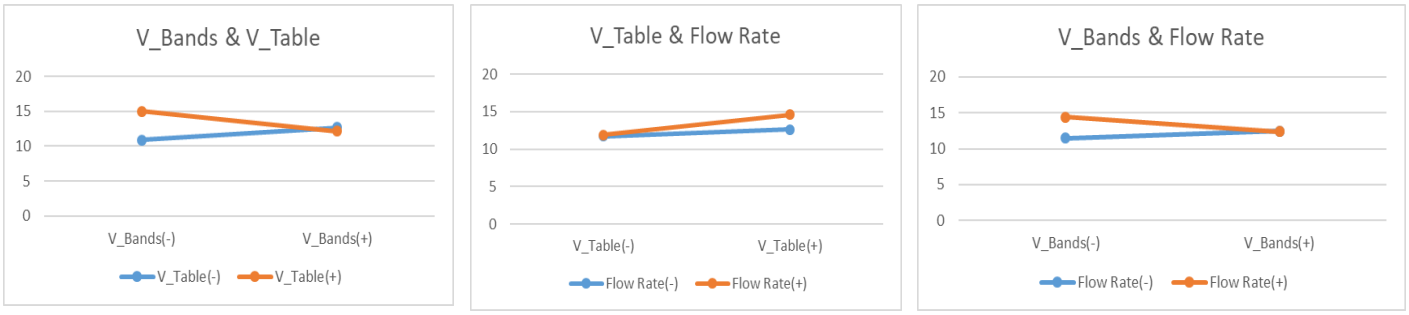

Fig. 10 - Interaction plots for the fibre diameter.

The fact that the measurements of the pore size took in consideration the smallest distance of the pore is probably the reason behind the difference on the calculation of the effect of the flow rate. The velocity of the deposition table, however, presents the higher effect on the pore sizes of the resulting fibre matrices, as it should be expected. As for the interaction between effects – Fig. 10 - it can be concluded that there is an interaction between all the combinations analysed and the most significant one is between the V_{bands} with V_{table}.

3.2. ANOVA Linear Regression vs. Theoretical Model

A linear equation was obtained with the coefficients calculated with ANOVA for each parameter and a constant K, which predicts the distance between the fibres (d_{fiber}) in [μm] after the electrospinning process, having as base the experimental results. In general, the linear regression equation – Eq. (5) - shows sufficiently good results in the prediction of the distance between the fibres, with a standard error for the regression of 4,746, which means the experimental values tend to differ from the ones predicted by the ANOVA model on about 4%.

$$d_{fiber} = 0.1196 \cdot V_{bands} + 1.285 \cdot V_{table} + 0.108 \cdot F - 0.959 \cdot (V_{bands} \cdot V_{table}) - \cdots \\ \ldots - 0.754 \cdot (V_{bands} \cdot F) + 1.272 \cdot (V_{table} \cdot F) - 0.663 \cdot (V_{bands} \cdot V_{table} \cdot F) + K \quad (5)$$

As shown previously, a Matlab theoretical model simulation was conducted to predict how the factors should influence the distance between the fibres. The graph on the left hand-side of Fig. 11 shows the comparison of the theoretical model with the experimental results. The variance on the results is noticeable, which was somewhat expected. While the results from the experiments vary from 10 to 25 µm, the theoretical model range of values goes from 10 to 120 µm. The difference is notorious, and it comes from the fact that, in theory, several external physical factors cannot be accounted. Moreover, the theoretical model assumes the three parameters have the same percentage of relevance on the results, and as seen previously on the statistical analysis, that is not the case.

The model can, however, predict how the variations on the input parameters will affect the distance between the fibres - increase it or decrease it. The theoretical model can also be optimized by adding some adjustment constants that consider the level of significance of each factor. The graph on the right hand-side of Fig. 11 shows the result when the theoretical equation is adapted by taking the effect of parameters into consideration. A significant change can be seen on the outcome results. However, it is still not an accurate prediction since there is a substantial variance between the experimental results and the model's prediction, having an overall average of error of 30%, which is a highly significant value for an error percentage. This outcome is to be expected since electrospinning is a highly complex process, and there are always external factors affecting the results that, in theory, cannot be accounted for. One factor that can be modified to improve the results of the current mathematical model, is the non-consideration that the table velocity is constant throughout its entire displacement, as the table inverts the movement between each deposition of fibres, taking time (acceleration) to reach the programmed velocity, this means that the fibres deposited in reality are at a shorter distance between them because the mean velocity is lower than programmed velocity.

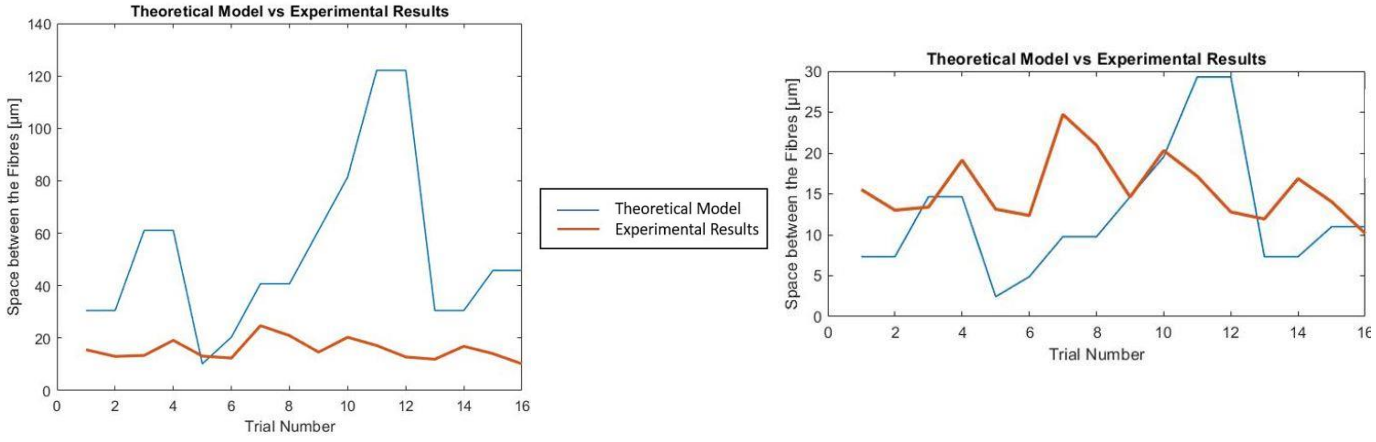

Fig. 11 – Comparison of the theoretical model with the ANOVA model (left) and comparison with the optimized theoretical model with the ANOVA model (right).

4. Discussion

Electrospinning is a simple, unique, versatile, and cost-effective technique widely used for the fabrication of aligned nanofibres [17]. The morphology of the nanofibres is significantly affected by the various parameters such as polymer concentration, viscosity, molecular weight, applied voltage, tip-to-collector distance, and solvent [9-15]. However, in the context of this work, different parameters were analysed to understand if, and how, they would affect specific characteristics of the resulting nanofibres mats. In summary, the three experimental factors, velocity of the collecting bands, the velocity of the deposition table and the flow rate, show significance for the distance between the fibres and the pore size in the obtained electrospun mesh. It is notorious that, for these two output variables, the parameter with higher effect on the results is the velocity of the deposition table, such that higher values of this parameter lead to bigger distance between the fibres and bigger pore sizes. The velocity of the collecting bands also showed similar effects on both the distance between the fibres and the pore size, such that higher values for this parameter lead to higher distance between the fibres and bigger pore sizes. The flow rate showed a negative effect on the distance between the fibres, such that increasing its value leads to smaller distance between the fibres. However, it shows an opposite behaviour on the pore size, having a positive effect. The reason behind these results probably lays on the fact that, electrospinning is sensible to many external factors as temperature, humidity, which cannot be accounted for, could have affected the pore size results. To reduce the randomness of the process, and consequently, the effect of the uncontrollable external factors, more experiments must be performed and accounted for in the statistical analysis.

The model resulting from an ANOVA statistical linear regression, which predicts the result of the distance between the fibres, presented excellent results. However, further optimisation should be conducted to reduce even more the error. This can be achieved by performing more experiments and inserting the resulting data into the ANOVA calculations. The same can be stated for the theoretical model developed. The model should take into consideration on how much each parameter affects the results and maybe, even consider the interaction existent between factors. This can be performed making use of the statistical analysis done throughout this work.

The study on how the various parameters of the electrospinning process affect its results is of great importance, since electrospun nanofibres have found numerous potential applications in almost every field, including enzyme immobilisation, sensing membranes, protective clothing, wound healing and of, course, bone, and cartilage tissue engineering. The study on how to control the alignment and distance of the nanofibres is essential since one of the limitations of the resulting electrospun nanofiber scaffolds is that cells show reduced infiltration into it. Controlling the arrangement, and thus the distance between the fibres is one step closer to the making of 3D scaffolds with the perfect pore sizes for cell infiltration. The ideal pore size for cartilage tissue engineering is not yet determined, however the native cartilage presents chondrocytes sizes around 15 μm [19], which assumes that a pore sizes greater than this value are sufficient to guarantee cell migration. The amplitude of the pore sizes obtained from all DoE experiments done was between 10 μm and 20 μm, which are in the range of the mean chondrocyte sizes reported. The results showed that the parameter with a more significant impact on the distance between the fibres, and consequently pore size, is the velocity of the deposition table. Thus, inserting a moving deposition module, with both linear and rotational movement, to electrospinning equipment is of great help to control the fibre alignment, allowing significant progress for the construction of tissue-engineered cartilage, since it facilitates the replication of the native tissue's complex fibrillar organisation. Thus, allowing to create engineered tissues with anisotropic mechanical properties, like the native tissue of cartilage.

Acknowledgments

The authors acknowledge the financial support through project POCI-01-0145-FEDER-028424-PTDC/EME-SIS/28424/2017, which was funded by the Operational Program for Competitiveness and Internationalization (COMPETE 2020) in its component FEDER and by Science and Technology Foundation (FCT) through the OE budget. The authors also thank to FCT for the PhD grant SFRH/BD/133129/2017.

References

[1] Johnstone B, Alini M, Cucchiarini M, Dodge GR, Eglin D, Guilak F, Madry H, Mata A, Mauck RL, Semino CE, Stoddart MJ. Tissue engineering for articular cartilage repair – the state of the art. Eur Cell Mater. 2013, 25, pp. 248-67.

[2] Bandeiras, C., Completo, A.M.G. Computational Modelling of Tissue-Engineered Cartilage Constructs. Lecture Notes in Computational Vision and Biomechanics, 2020, 35, pp. 203–222.

[3] Bandeiras, C., Completo, A. A mathematical model of tissue-engineered cartilage development under cyclic compressive loading. Biomechanics and Modeling in Mechanobiology, 2017, 16(2), pp. 651–666.
[4] Bandeiras, C., Completo, A., Ramos, A. Influence of the scaffold geometry on the spatial and temporal evolution of the mechanical properties of tissue-engineered cartilage: insights from a mathematical model. Biomechanics and Modeling in Mechanobiology, 2015, 14(5), pp. 1057–1070.
[5] Bandeiras, C., Completo, A. Comparison of mechanical parameters between tissue-engineered and native cartilage: A numerical study. Computer Methods in Biomechanics and Biomedical Engineering, 2015, 18, pp. 1876–1877.
[6] Bandeiras, C., Completo, A., Ramos, A., Ferreira, J.P., Mendes, A.F. Tissue Engineered Cartilage in Unconfined Compression: Biomechanical Analysis. Materials Today: Proceedings, 2015, 2(1), pp. 355–364.
[7] Bandeiras, C., Completo, A., Ramos, A. Compression, shear and bending on tissue-engineered cartilage: a numerical study. Computer Methods in Biomechanics and Biomedical Engineering, 2014, 17, pp. 2–3
[8] Completo, A., Bandeiras, C., Fonseca, F. Comparative assessment of intrinsic mechanical stimuli on knee cartilage and compressed agarose constructs. Medical Engineering and Physics, 2017, 44, pp. 87–93.
[9] N. S. Binulal, A. Natarajan, D. Menon, V. K. Bhaskaran, U. Mony, and S. V. Nair. PCL gelatin composite nanofibres electrospun using diluted acetic acid-ethyl acetate solvent system for stem cell-based bone tissue engineering. J Biomater Sci Polym Ed. 2014, 25, pp. 325-340.
[10] K. Ren, Y. Wang, T. Sun, W. Yue, and H. Zhang. Electrospun PCL/gelatin composite nanofibre structures for effective guided bone regeneration membranes. Materials Science and Engineering C. 2017, 78, pp. 324-332.
[11] Semitela, Â., Girão, A.F., Fernandes, C., ...Completo, A., Marques, P.A.A.P. Electrospinning of bioactive polycaprolactone-gelatin nanofibres with increased pore size for cartilage tissue engineering applications. Journal of Biomaterials Applications, 2020, 35(4-5), pp. 471–484
[12] Girão, A.F., Semitela, Â., Pereira, A.L., Completo, A., Marques, P.A.A.P. Microfabrication of a biomimetic arcade-like electrospun scaffold for cartilage tissue engineering applications. Journal of Materials Science: Materials in Medicine, 2020, 31(8), 69.
[13] Girão, A.F., Semitela, Â., Ramalho, G., Completo, A., Marques, P.A.A.P. Mimicking nature: Fabrication of 3D anisotropic electrospun polycaprolactone scaffolds for cartilage tissue engineering applications. Composites Part B: Engineering, 2018, 154, pp. 99–107
[14] Cortez, S., Freitas, F.L., Completo, A., Alves, J.L. A 3D finite element model to predict the arcade-like collagen structure in a layered PCL scaffold for cartilage tissue engineering. Computer Methods in Biomechanics and Biomedical Engineering, 2017, 20, pp. 47–48
[15] Girão, A.F., Gonçalves, G., Bhangra, K.S., Completo, A., Marques, P.A.A.P. Electrostatic self-assembled graphene oxide-collagen scaffolds towards a three-dimensional microenvironment for biomimetic applications. RSC Advances, 2016, 6(54), pp. 49039–49051.
[16] Meng Q, An S, Damion, RA, Jin Z, Wilcox R, Fisher J, Jones A. The effect of collagen fibril orientation on the biphasic mechanics of articular cartilage. Journal of the Mechanical Behavior of Biomedical Materials (2017).
[17] Completo, A., Marques P. Automated manufacturing of three-dimensional cell matrices with nanofibres of controlled alignment and uniform cell distribution. Patent pending - European Patent: EP21160776.7 de 04/03/2021.
[18] Zheng, R., Duan, H., Xue, J., Liu, Y., Feng, B., Zhao, S., Zhu, Y., Liu, Y., He, A., Zhang, W., Liu, W., Cao, Y., Zhou, G.. The influence of Gelatin/PCL ratio and 3-D construct shape of electrospun membranes on cartilage regeneration. Biomaterials, 2014, 35, pp. 152–164.
[19] Hirsch, M.S., Cook, S.C., Killiany, R., Hartford Svoboda, K.K. Increased cell diameter precedes chondrocyte terminal differentiation, whereas cell-matrix attachment complex proteins appear constant. The Anatomical Record, 1996, 244, 284–296.